# JGR Space Physics

**Key Points:**
- Westward propagation of the EMIC wave generation region is due to both the substorm expansion and azimuthal drift of injected protons
- Strong pitch-angle diffusion regime is confirmed by observations of proton fluxes at low altitude and the diffusion coefficient calculation
- The diffusion coefficient maximum corresponds well to the energy range of the observed proton precipitation

# Evening Side EMIC Waves and Related Proton Precipitation Induced by a Substorm

A. G. Yahnin[1] [image], T. A. Popova[1] [image], A. G. Demekhov[1,2] [image], A. A. Lubchich[1] [image], A. Matsuoka[3] [image], K. Asamura[3] [image], Y. Miyoshi[4] [image], S. Yokota[5] [image], S. Kasahara[6] [image], K. Keika[6] [image], T. Hori[4] [image], F. Tsuchiya[7] [image], A. Kumamoto[7] [image], Y. Kasahara[8] [image], M. Shoji[4] [image], Y. Kasaba[7] [image], S. Nakamura[4] [image], I. Shinohara[3] [image], H. Kim[9] [image], S. Noh[9] [image], and T. Raita[10] [image]

[1]Polar Geophysical Institute, Apatity, Russia, [2]Institute of Applied Physics of the RAS, Nizhny Novgorod, Russia, [3]JAXA, Sagamihara, Japan, [4]Institute for Space-Earth Environmental Research, Nagoya University, Nagoya, Japan, [5]Osaka University, Osaka, Japan, [6]The University of Tokyo, Tokyo, Japan, [7]Tohoku University, Sendai, Japan, [8]Kanazawa University, Kanazawa, Japan, [9]New Jersey Institute of Technology, Newark, NJ, USA, [10]Sodankylä Geophysical Observatory, University of Oulu, Sodankylä, Finland

**Abstract** We present the results of a multi-point and multi-instrument study of electromagnetic ion cyclotron (EMIC) waves and related energetic proton precipitation during a substorm. We analyze the data from Arase (ERG) and Van Allen Probes (VAPs) A and B spacecraft for an event of 16 and 17 UT on December 1, 2018. VAP-A detected an almost dispersionless injection of energetic protons related to the substorm onset in the night sector. Then the proton injection was detected by VAP-B and further by Arase, as a dispersive enhancement of energetic proton flux. The proton flux enhancement at every spacecraft coincided with the EMIC wave enhancement or appearance. This data show the excitation of EMIC waves first inside an expanding substorm wedge and then by a drifting cloud of injected protons. Low-orbiting NOAA/POES and MetOp satellites observed precipitation of energetic protons nearly conjugate with the EMIC wave observations in the magnetosphere. The proton pitch-angle diffusion coefficient and the strong diffusion regime index were calculated based on the observed wave, plasma, and magnetic field parameters. The diffusion coefficient reaches a maximum at energies corresponding well to the energy range of the observed proton precipitation. The diffusion coefficient values indicated the strong diffusion regime, in agreement with the equality of the trapped and precipitating proton flux at the low-Earth orbit. The growth rate calculations based on the plasma and magnetic field data from both VAP and Arase spacecraft indicated that the detected EMIC waves could be generated in the region of their observation or in its close vicinity.

**Plain Language Summary** Electromagnetic ion cyclotron (EMIC) waves are believed to play a significant role in the dynamics of energetic protons and relativistic electrons in the Earth's magnetosphere. The properties of these waves are being intensively studied. We consider the conditions of the EMIC wave generation and the dynamics of the wave source during a substorm event using a unique configuration of three spacecraft (Arase and two Van Allen Probes). All spacecraft were at approximately the same distance from the Earth, forming a chain across the evening local time sector. Analyzing parameters of the wave generation obtained from in situ measured proton distribution function, we came to the conclusion that the waves could be generated within the substorm area, sometimes close to, but not necessary at the spacecraft location. As the substorm expands in longitude, the EMIC wave source exhibits a longitudinal drift. When substorm expansion stops, the wave generation region expands due to the magnetic drift of protons injected during the substorm. The observed wave properties show that the waves are able to precipitate energetic protons into the atmosphere. This is confirmed by observations of low orbiting satellites measuring proton precipitating fluxes.

## 1. Introduction

Electromagnetic ion cyclotron (EMIC) waves in the magnetosphere are known to be generated by the cyclotron instability of anisotropic distributions of energetic (1–100 keV) protons (e.g., Kennel & Petschek, 1966; Sagdeev & Shafranov, 1961) constituting the ring current and plasma sheet populations. The growth rate of the instability is determined by the magnetic field strength, hot proton flux, energy, temperature anisotropy,

and plasma density. In the source region, these waves have left-hand polarization and low wave normal angles that enable their resonant interaction with energetic protons and relativistic electrons. Such interaction may play an important role in the magnetospheric dynamics, especially in the loss processes of relativistic electrons and energetic protons from the radiation belt and ring current (e.g., Bespalov et al., 1994; Cornwall et al., 1970; Jordanova et al., 2001, 2008; Kennel & Petschek, 1966; Kim et al., 2021; Miyoshi et al., 2008; Semenova et al., 2019; Shreedevi et al., 2021; Thorne & Kennel, 1971; Yahnin & Yahnina, 2007). Thus, it is important to study both the internal magnetospheric plasma conditions which are appropriate for the EMIC wave generation as well as external factors that rule their occurrence and intensity. As known, the morphological features of the EMIC waves and EMIC wave-associated precipitation of energetic particles are controlled by geomagnetic activity through the generation of the enhanced flux of hot protons in the inner magnetosphere (Chen et al., 2020; Halford et al., 2010, 2016; Keika et al., 2013; Meredith et al., 2014; Saikin et al., 2016; Semenova et al., 2019; Usanova et al., 2012) and by the solar wind dynamic pressure through the magnitude of the magnetic field and associated proton temperature anisotropy as well as through the reconfiguration of magnetic field lines and associated drift-shell splitting and Shabansky orbits (e.g., Chen et al., 2020; McCollough et al., 2010; Olson & Lee, 1983; Popova et al., 2010; Saikin et al., 2016; Semenova et al., 2019; Shabansky, 1971; Usanova et al., 2010, 2012; Usanova and Mann, 2016; Yahnin et al., 2019).

One of the manifestations of geomagnetic activity is substorms, which produce injections of energetic protons. It is well known that substorms are often followed by the dusk-side EMIC waves. This follows from ground observations of IPDP (Intervals of Pulsations of Diminishing Periods) and Pc1-Pc2 (quasi-monochromatic continued pulsations in the range from 0.1 to several Hz), which are the ground signatures of EMIC waves (e.g., Kangas et al., 1998). For example, Yahnin et al. (2009) showed a close relation of the IPDP on the ground with the westward drifting proton "clouds" (DeForest and McIlwain, 1971) injected on the night-side and observed by geosynchronous LANL spacecraft.

Remya et al. (2018) demonstrated that the appearance of the substorm-related EMIC waves at a spacecraft location does coincide with the arrival of the proton cloud injected in the late evening sector. Selecting "pure" injection-related EMIC waves (i.e., occurred during substorms, but not related to either solar wind pressure enhancements or geomagnetic storms), Remya et al. (2019) collected 145 such events observed during 2015 by the Van Allen Probes (VAPs). They found that the occurrence of the injection-related EMIC waves reaches a maximum in the afternoon-dusk sector (14–17 MLT). Similar morphological feature has also been revealed by Jun et al. (2019a, 2019b), who considered EMIC waves associated with proton injections which were selected without division to storm, non-storm, and solar wind pressure-related events. Using the Arase data, Matsuda et al. (2018) found a clear afternoon peak in the occurrence probability of unstructured EMIC waves in the region of $L = 5$–$9$ and noted that this peak can be explained by the well-recognized theory of the drift path of fresh ring-current ions. Similar feature (afternoon-evening maximum in EMIC wave occurrence) was also found based on statistical analysis of data from many other missions (e.g., Halford et al., 2016; Keika et al., 2013; Meredith et al., 2014; Saikin et al., 2015; Usanova et al., 2012).

Some authors investigated EMIC wave properties and local field and plasma conditions related to observations of the EMIC waves in space based on the case (e.g., Lyubchich et al., 2017; Min et al., 2015; Zhang et al., 2014) and statistical studies (e.g., Allen et al., 2016; Jun et al., 2019b; Noh et al., 2018; Saikin et al., 2018). In particular, the density of the cold plasma is an important parameter affecting the threshold of the ion-cyclotron instability (e.g., Gary et al., 1994; Kennel & Petschek, 1966; Kozyra et al., 1984; Lubchich & Semenova, 2015; Trakhtengerts & Rycroft, 2008). Jun et al. (2019a, 2019b) investigated EMIC waves in He+ and H+ bands observed by VAPs in relation to hot H+ injections and cold plasmaspheric plasma. They found that injection-related EMIC waves in the He+ band are mainly generated inside the plasmasphere. In contrast, waves in the H+ band mostly appear outside the plasmasphere and they follow the enhancements of the solar wind dynamic pressure. At the same time, as noted by Remya et al. (2018), there are few papers dealing with space-borne observations of the plasma and electromagnetic fields suitable to study conditions during the generation of the injection-induced EMIC waves.

EMIC waves generated by the ion-cyclotron instability may scatter hot protons into the loss cone. The proton precipitation related to the EMIC waves was described, for example, by Engebretson et al. (2015), Miyoshi et al. (2008), Popova et al. (2018), Søraas et al. (1980), Yahnin et al. (2018), and many others. Some authors calculated the pitch-angle diffusion coefficient based on in situ wave and plasma parameters. Thus,
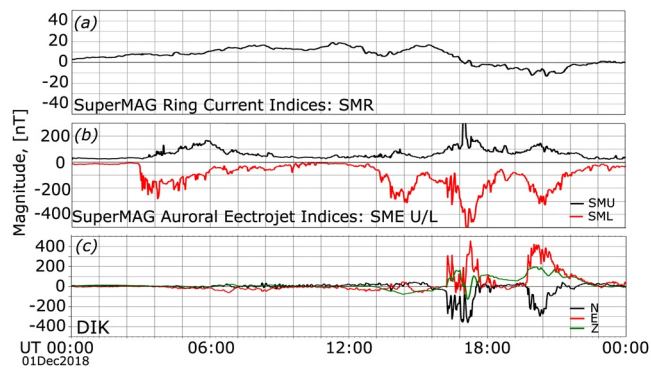
**Figure 1.** Summary plot for geomagnetic field parameters for the entire day of December 1, 2018. The SuperMAG Ring Current index (SMR) (a), the SuperMAG Auroral Electrojet Index (black line— the maximum eastward auroral electrojet strength (SMU), red line—the maximum westward auroral electrojet strength (SML)) (b), the magnetic field disturbances at the station Dixon (black line—the local magnetic north component, red line—the local magnetic east component, and green line—the vertically down component) (c).

using the parameters observed by the Cluster spacecraft within the plasmaspheric plume Xiong et al. (2016) calculated the pitch angle diffusion coefficients for ring current protons and demonstrated that EMIC waves could be responsible for the ion scattering and loss-cone filling. Moreover, these authors concluded the strong pitch-angle diffusion of protons in the wide range of energies. Using the plasma parameters and spectral intensity of the EMIC waves observed onboard the THEMIS spacecraft, Popova et al. (2020) calculated the pitch-angle diffusion coefficient of energetic protons at low pitch angles and compared the result with energies of precipitating protons observed at low altitudes by POES satellites. The energy range where the diffusion coefficient maximizes was found to be in qualitative agreement with typical energies of precipitating protons (from a few to tens of keV).

Comparison of the observed characteristics of the precipitating protons with the characteristics deduced based on the pitch-angle diffusion coefficient calculations and determination of the diffusion regimes are important, in particular, for the development of the methods for inferring the EMIC wave amplitude from the observations of the precipitating protons (e.g., Zhang et al., 2017). It is worth noting that such comparisons are scanty in the current literature. Thus, it is important to study more events for which such a comparison could be performed and understand their specific features from a common physics point of view.

In this report, we present the results of a comprehensive study of EMIC waves and related precipitation of protons based on multi-instrument and multi-point observations onboard three inner magnetosphere spacecraft and some low-orbiting satellites in the pre-midnight and evening sector. This event (16 and 17 UT on December 1, 2018) is closely related to a substorm proton injection in a non-storm time; In this respect, it is similar to the event considered by Remya et al. (2018). At the same time, the event studied here occurred during rather high (5–6 nPa) solar wind dynamic pressure, in contrast with 1–2 nPa in study by Remya et al. (2018), their Figure 1). Also, our observations took place after rather intense geomagnetic activity that produced a high level of the proton flux in the inner magnetosphere.

The spacecraft instrumentation and the data used in this study are described in Section 2. The results of observations in the magnetosphere are given in Sections 3.1–3.4, and low altitude observations of the proton precipitation are presented in Section 3.5. In Section 4, we discuss the observations and, in particular, present the calculations of the EMIC growth rate and pitch-angle diffusion coefficients. Summary and conclusions are given in Section 5.

## 2. Instruments and Data

This study is based on the data from multiple spacecraft and instruments briefly described below. In the magnetosphere, the measurements of fields and particles were performed by the two identically instrumented spacecraft VAPs (formerly known as Radiation Belt Storm Probes, RBSP) A and B (VAP-A and VAP-B) and by the Arase spacecraft (formerly known as Exploration of energization and Radiation in Geospace, ERG). A constellation of the NOAA Polar Orbiting Environmental Satellites (POES) and European Organization for the Exploitation of Meteorological Satellites (EUMETSAT) Meteorological Operational (MetOp) satellites at low Earth orbits (LEO) provided the information on the particle precipitation. In addition, we used selected auroral images obtained from the Defense Meteorological Satellite Program (DMSP) satellites. Some ground-based magnetometer data along with solar wind parameters from OMNI data set integrated into the SuperMAG database (Gjerloev, 2012; Newell & Gjerloev, 2011) were also used in this study as well as the information on the magnetometer observations at the station Istok, which is one of the stations of the PWING (study of dynamical variation of Particles and Waves in the INner magnetosphere using Ground-based network observations) project (Shiokawa et al., 2017).

### 2.1. Van Allen Probes

The VAPs spacecraft (the mission started in August 2012 and ended in October 2019) had an orbital period of ∼9 h, a perigee at ∼1.1 $R_E$, an apogee at ∼5.8 $R_E$, and orbit inclination of 10.2° (Mauk et al., 2013). We analyze the particle behavior based on the data from the Helium, Oxygen, Proton, and Electron (HOPE) instrument (Funsten et al., 2013) and the Radiation Belt Storm Probe Ion Composition Experiment (RB-SPICE) (Mitchell et al., 2013). They measured protons within the energy range of 0.001–50 and 50–600 keV, respectively. Both instruments allow one to obtain the pitch-angle distribution of particles in a number of energy ranges as well as omnidirectional fluxes. The magnetic field data were provided by the fluxgate magnetometer which is a part of the Electric and Magnetic Field Instrument Suitr and Integrated Science (EMFISIS) (Kletzing et al., 2013). We used magnetometer data with a sampling rate of 64 Hz to reveal the EMIC waves in the dynamic spectra of the magnetic fluctuations. The ambient magnetic field data are used in calculation of the ion gyrofrequencies, pitch-angle distribution, EMIC wave growth rate, and pitch-angle diffusion coefficients. The cold plasma density needed for the calculations was obtained from the upper hybrid resonance (UHR) frequency measurements also provided by EMFISIS. Electric field 64-Hz data are provided by the Electric Fields and Waves (EFW) instruments (Wygant et al., 2013).

### 2.2. Arase (ERG)

The Arase spacecraft was launched in December 2016. Its orbital period is ∼9.5 h, a perigee is 400 km, an apogee is about 6 $R_E$, and orbit inclination is 31°(Miyoshi, Shinohara, Takashima, et al., 2018). The low-energy particles experiments-ion mass analyzer (LEP-i) and medium-energy particle experiments-ion mass analyzer (MEP-i), which data are used in this study, can measure ions from 10 eV/q to 180 keV/q with mass discrimination. The LEP-i instrument (Asamura, Kazama, et al., 2018; Asamura, Miyoshi, et al., 2018) has an upper limit of 25 keV/q, and the lower energy limit of MEP-i (Yokota et al., 2017, 2019) is 10 keV/q.

The magnetic field experiment (MGF) measures magnetic fields from DC to several tens of Hz (the maximum burst sampling frequency is 256 Hz). That is, the MGF can measure the background field strength and direction, and ultra-low frequency (ULF) waves including EMIC waves (Matsuoka, Teramoto, Nomura, et al., 2018). We use 64-Hz MGF data in our study (Matsuoka, Teramoto, Imajo, et al., 2018). Electric field 64-Hz data are provided by the electric field detector (EFD) of the plasma wave experiment (PWE) (Kasaba et al., 2017; Kasahara, Kasaba, et al., 2018; Kasahara et al., 2020). The cold plasma density was estimated from the UHR frequency measurements provided by PWE High-Frequency Analyzer (HFA) (Kumamoto et al., 2018; Kasahara, Kumamoto, et al., 2018).

### 2.3. POES/MetOp

The POES and MetOp satellites carry identical sets of instruments for monitoring the Earth's surface and atmosphere. Among others, each set includes the Space Environment Monitor-2 (SEM-2) instrument suite, including the total energy detector (TED) and the Medium Energy Protons and Electrons Detector (MEPED) (Evans & Greer, 2004). TED measures electrons and protons in the energy range of 0.05–20 keV with two detectors having a narrow aperture; one is aligned along the zenith direction of the satellite (0° detector) and another is aligned 30° off the zenith direction (30° detector). TED measures particles in 16 energy channels, but the products of the instrument are the total energy flux calculated onboard and the differential flux from only four channels (∼0.2, ∼0.8, ∼2.5, and ∼8 keV).

To measure charged particles with energies $E > 30$ keV, NOAA POES and MetOp satellites are equipped with the Medium Energy Proton and Electron Detector (MEPED). This instrument consists, particularly, of two pairs of directional telescopes. The telescopes are oriented such that the sample from the local vertical (zenith) and horizontal ("backward" along the direction of travel) fields of view (0° and 90° telescopes, respectively). In the auroral and subauroral regions, the 0° telescopes measure precipitating particles (within the loss cone), while the 90° telescopes measure predominantly trapped particles (e.g., Rodger, Clilverd, et al., 2010; Rodger, Carson, et al., 2010). The electron telescopes have three nominal energy channels: E1 (>30 keV), E2 (>100 keV), and E3 (>300 keV). Proton directional telescopes are designed to measure ions in six energy channels: P1 (30–80 keV), P2 (80–250 keV), P3 (250–800 keV), P4 (800–2,500 keV), P5 (2,500–6,900 keV), and P6 (>6.9 MeV). The channel P6 equally responds to >1 MeV electrons, thus (since the

>6.9 MeV protons are rarely present) this channel is often used as the fourth (relativistic) electron channel E4 (e.g., Miyoshi et al., 2008; Yando et al., 2011). In this study, we will use the measurements of the proton differential flux from the abovementioned TED channels and channels P1–P3 from MEPED.

### 2.4. DMSP SSUSI

The Special Sensor Ultraviolet Spectrographic Imager (SSUSI) is a part of the instrumentation of some latest Defense Meteorological Satellite Program (DMSP) satellites. These satellites have nearly polar, sun-synchronous orbits at an altitude of about 850 km. Their orbital period is some 102 min. In particular, the SSUSI measures ultraviolet (UV) emissions from auroras in five different wavelength bands: HI 121.6 nm, OI 130.4 nm, OI 135.6 nm, $N_2$ Lyman-Birge-Hopfield bands from 140.0 to 150.0 nm (LBH short), and from 165.0 to 180.0 nm (LBH long). The auroral images are obtained using a sequence of horizon to horizon scans transversely to the orbit direction (Paxton et al., 2002).

## 3. Observation Results

### 3.1. Substorm of 16:13 UT on December 1, 2018

The SuperMAG Ring Current index (an analog of SYM-H and Dst indices; Newell & Gjerloev, 2012) was less than 20 nT in absolute value during the entire day of December 1, 2018, and only 7 nT during the hour 16 and 17 UT (Figure 1a). According to the SuperMAG Auroral Electrojet Index (Newell & Gjerloev, 2011) (Figure 1b), a substorm activity was detected at 03–06 UT, at 13–15 UT, and after 16 UT. In particular, at 1613 UT, after an interval of the relative geomagnetic quietness, the disturbances of the magnetic field including negative bays in the northward component (up to −300 nT) (which indicate the explosive activations of the westward electrojet in the night sector) were detected at Dixon (MLat = 69.36, MLT = 22.13), see Figure 1c. Similar variations of the magnetic field and strong burst of irregular geomagnetic pulsations were also observed at station Istok (MLat = 66.2, MLT = 22.2) (Beletskii et al., 2019). Such signatures clearly signal on the development of the substorm expansion phase (e.g., Rostoker et al., 1980).

The substorm development is confirmed by the aurora observations with the SSUSI instrument onboard the DMSP F-17 and F-18 satellites. The satellites crossed the evening part of the auroral oval at around 16:05 UT (just before the substorm onset), around 16:17 UT (soon after the onset), and around 16:40 UT. The corresponding auroral images in the LBHL band (produced by precipitating electrons) and HI 121.6 nm (proton aurora) are shown in Figures 2a and 2b, respectively. The auroral images do not show the entire auroral bulge. However, the second and third plots in Figure 2a clearly demonstrate the development of the westward traveling surge (WTS) in the evening sector. This feature is also a signature of the auroral substorm (e.g., Akasofu, 1977; Rostoker et al., 1980).

In Figure 2a, the approximate ionospheric projections of the three magnetospheric spacecraft are also shown. One can see that by ~16:17 UT, the meridian of the VAP-A spacecraft was already occupied by the auroral bulge, and by ~1640 UT, the WTS propagated through the VAP-B meridian. Subsequent DMSP images (not shown) indicate that WTS stopped and decayed. It seems that this substorm did not expand to the Arase meridian because the IMAGE magnetometers in Scandinavia and Kola Peninsula, where the spacecraft was mapped to, did not reveal any signatures of the westward electrojet up to ~20 UT (not shown). The third image (~16:40 UT) in Figure 2b shows the emergence of a proton aurora structure equatorward of the auroral bulge. There is no similar structure in the electron auroras.

In Figures 2c and 2d, maps of the orbits of VAP and Arase spacecraft along with some traces of NOAA POES and MetOp satellites are shown in L-MLT coordinates for the interval 16 and 17 UT (L is the McIlwain parameter, MLT is Magnetic Local Time; mapping has been done with use of the International Geomagnetic Reference Field (IGRF-13) (Alken et al., 2021) as internal magnetic field model and with external magnetic field model by Tsyganenko (1989) for $Kp$ = 2). In particular, MLT of VAP-A varied from 21.4 to 22.1 and the L-shell changed from 5.95 to 5.35. At the substorm onset, VAP-A was at $L$ = 5.85 and MLT = 21.5.
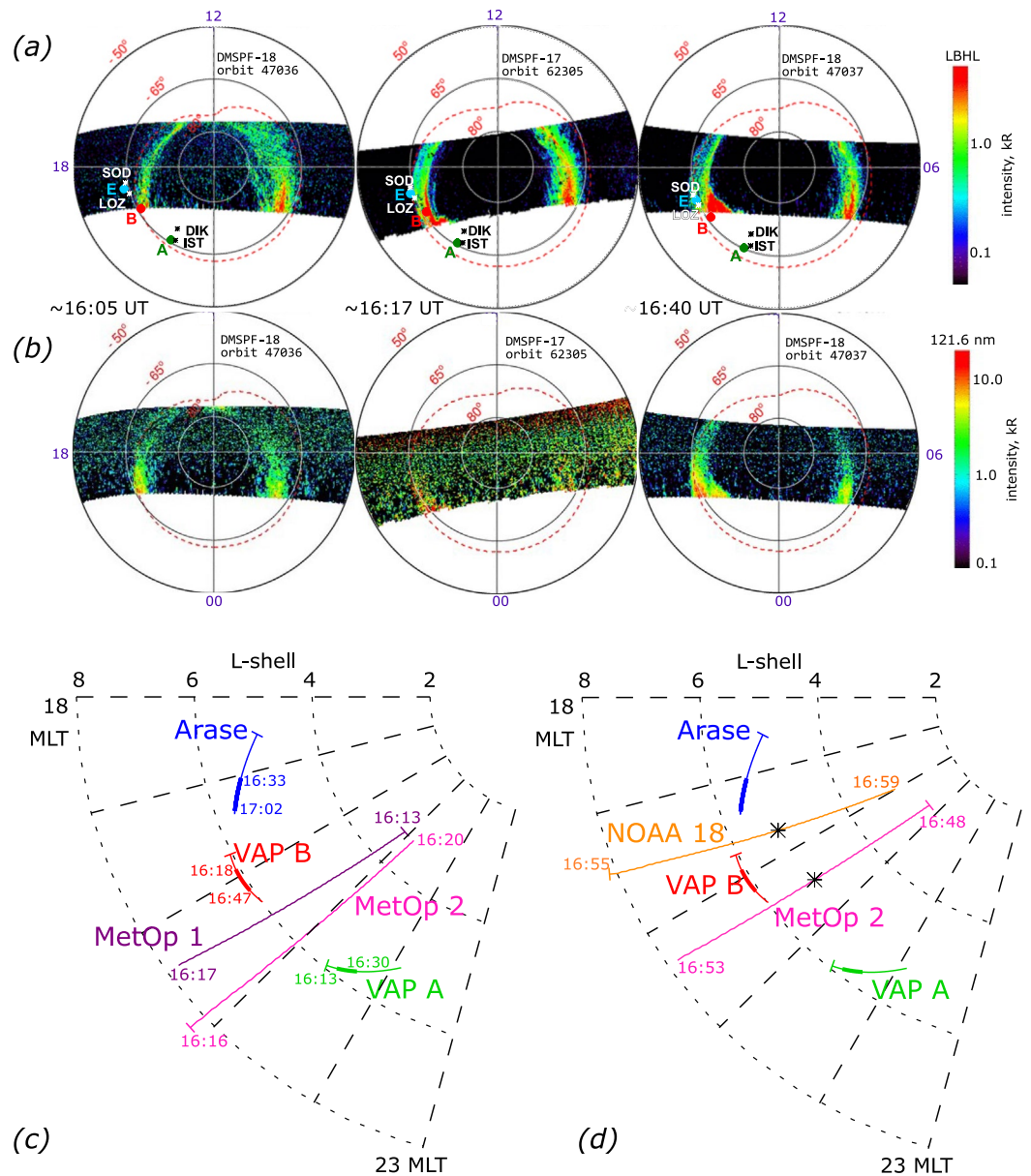
**Figure 2.** (a) Selected auroral images from DMSP/SSUSI in LBH-L (165–180 nm) band made during the interval 16 and 17 UT on December 1, 2018. The images show the development of the auroral substorm. Green, red, and cyan circles mark approximate positions of ionospheric projections of magnetospheric spacecraft in MLat-MLT coordinates: "A" – VAP-A, "B" – VAP-B, "E" – Arase/ERG. Red dashed line shows the equatorward boundary of the auroral oval according to the model by Zhang and Paxton (2008). White stars indicate locations of Lovozero (LOZ) and Sodankylä (SOD) ground stations. Black stars indicate locations of Dixon (DIK) and Istok (IST) stations. (b) The same as (a), but for images in the HI line (121.6 nm). (c, d) Trajectories of the satellites during the interval 16 and 17 UT on December 1, 2018 in L - MLT coordinates. On all traces, the dash marks the starting position. Thick segments on the trajectories of magnetospheric spacecraft corresponded to the time intervals (indicated on panel (c)) when the EMIC waves were detected. For the low-altitude satellites MetOp-1, MetOp-2, and NOAA-18, the initial and end time moments are indicated. The asterisk on the NOAA-18 trace (on panel (d)) marks the location for which the energy spectra of precipitating protons are shown in Figure 7.

### 3.2. Proton Fluxes Onboard VAP-A and Substorm Injection

Omnidirectional fluxes of protons detected by ECT HOPE and RBSPICE instruments onboard VAP-A are shown in Figures 3a and 3b for the interval 10–20 UT and with better time resolution in Figures 4a and 4b for the interval 16 and 17 UT. The data in Figures 3 and 4 demonstrate various proton populations
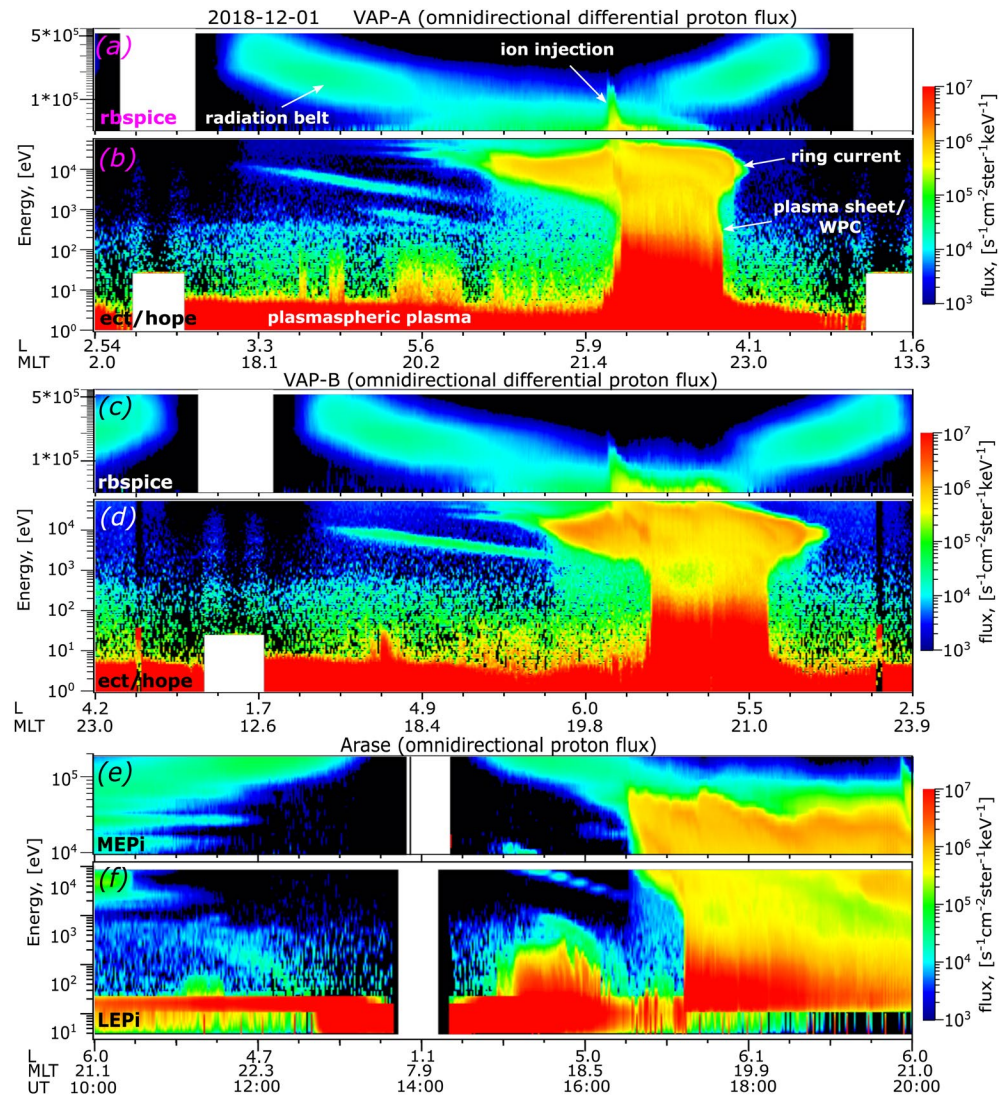
**Figure 3.** Energy spectra of omnidirectional proton fluxes measured by RBSPICE (a, c) and ECT/HOPE (b, d) onboard VAP-A (a, b) and VAP-B (c, d), and by MEP-i (e) and LEP-i (f) onboard Arase for the interval 10–20 UT on December 1, 2018. White rectangles correspond to the data absence.

at the spacecraft location. Protons with energies >100 keV constitute the radiation belt population at lower L-shells (e.g., Yue et al., 2017). Another population has energies in the range of ∼3–30 keV, and can be considered the ring current population. The spectrogram represents "nose structures" which are believed to be the result of both the preceding convection of plasma sheet protons and substorm injections (e.g., Ganushkina et al., 2000; Smith and Hoffman, 1974; Vallat et al., 2007). As shown in Figure 4b, the substorm that started at ∼16:13 UT lead to a step-like decrease of the mean energy of this population which could be interpreted as a pulsed shift of the ring current to the Earth and the approaching of the spacecraft location by the outer part of the ring current population.

The third population of protons has the energies of tens to hundreds eV, and this population can be related to either the innermost part of the plasma sheet (remnant layer (Feldstein & Galperin, 1985) or the warm plasma cloak (WPC) (Chappell et al., 2008)), or their mixture. The dynamics of these particles also correlates with the substorm development. In contrast to the ring current particles, the energy of this population increases, again in a step-like manner. Note that such pulsed development is a typical substorm feature (e.g., Sergeev & Yahnin, 1979; Yahnin et al., 1983). This energy increase can be interpreted as a shift of the
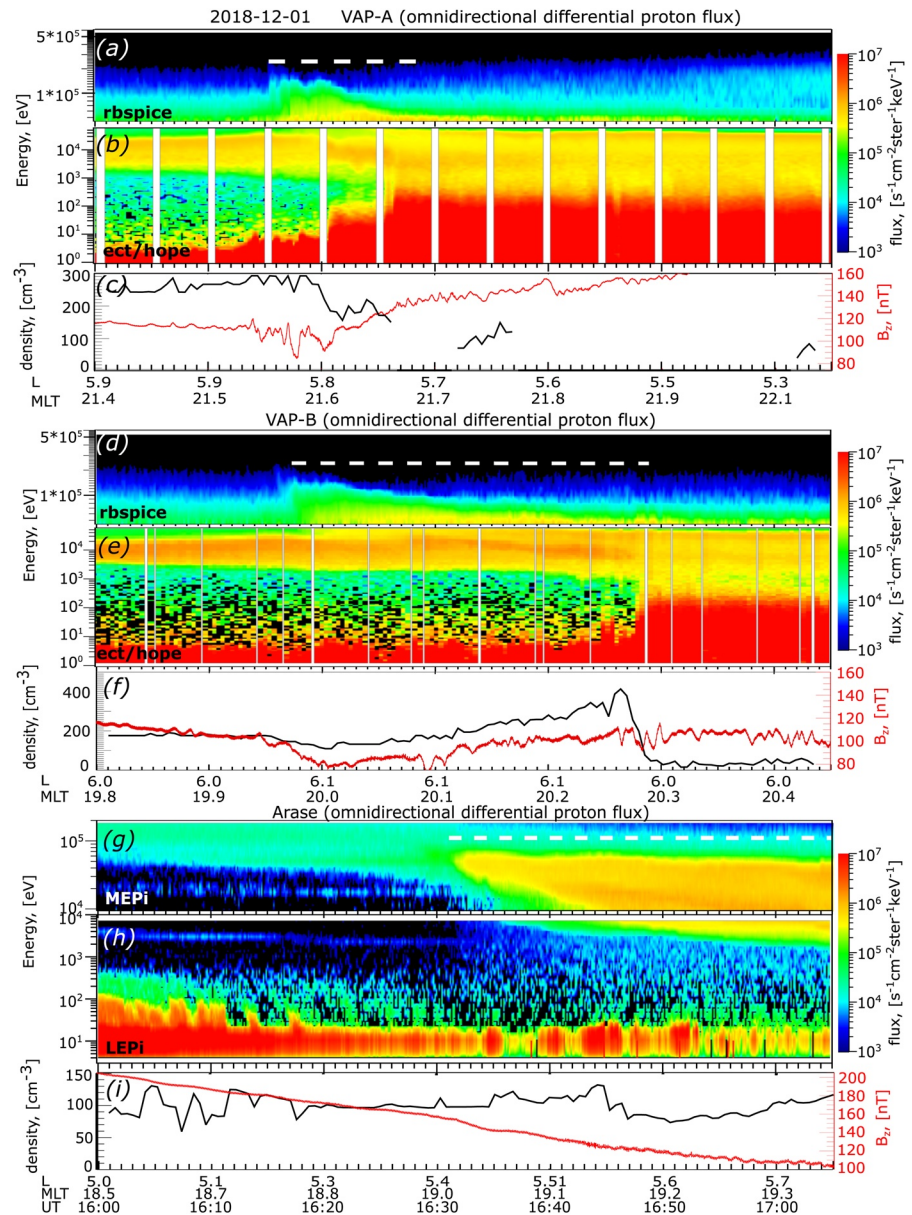
**Figure 4.** (a, b, d, e, g, h) Same as Figure 3, but with better time resolution (16:00–17:05 UT). (c, f, i) Cold plasma density for VAP-A, VAP-B, and Arase, respectively, calculated from the upper hybrid resonance frequency (black lines) and variations of the GSM Bz component of the ambient magnetic field at each spacecraft (red lines). White dashed horizontal lines on panels (a, d, g) show intervals of EMIC wave observations by each spacecraft (see Figure 5). White vertical bands on panels (b, e) and gaps in the plot on panel (c) correspond to data absence.

plasma sheet's inner edge to the Earth (in the inner plasma sheet the low-energy protons penetrate close to the Earth than higher energy protons due to concurrent electric and magnetic drifts).

The fourth plasma population which is seen at the VAP-A location is the plasmaspheric cold plasma. The cold plasma density just before the substorm onset was some 250–300 cm$^{-3}$. Soon after the substorm onset, one can see some drops in the plasma density coinciding with the step-like appearance of the plasma sheet/WPC particles and pulsed decrease of the energy of the ring current protons. Evidently, it means that the spacecraft detects the plasmasphere/plasma sheet transition boundary, which shifts inward. Close co-location of the plasmapause and the innermost plasma sheet has been often noted (e.g., Fairfield & Viñas, 1984).

One more population is attributed to the so-called substorm injection (e.g., Birn et al., 1997; Reeves, 1998), which is seen at energies ~50 to ~180 keV right after the substorm onset. This is pure ion injection, since the HOPE and RBSPICE electron data (not shown) do not yield any signatures of energetic electron injection. This happens when the spacecraft is at the western periphery of the injection area (Reeves et al., 1991). This agrees with the longitudinal position of the spacecraft relative to the WTS shown in Figure 2a. The injection consists of multiple bursts (with a minute time scale), which show very week energy dispersion suggesting the source of the particles not far eastward of the VAP-A. This weak dispersion is seen in RBSPICE channels, and it is hidden in the HOPE channels due to the pre-existing "nose-structure" particles. The injection seen in the RBSPICE data lasts from a few to some 10 min depending on the energy of protons. The higher energy protons quickly disappear, and since 16:25 UT the rest of the injection is only seen in HOPE data as protons, which energy graduate decreases to ~30 keV. This energy decrease is evidently due to the azimuthal drift of protons from the central and eastern parts of the injection region where the energy of injected protons is lower than at the periphery (e.g., Birn et al., 2013; Yahnin et al., 1996). At the spacecraft location, these newly injected protons substitute the "old" ring current population.

### 3.3. Progressive Development of the Proton Flux Enhancement Through the Pre-Midnight to Dusk Sector

The VAP-B spacecraft, which was located at $L \sim 6$ and MLT = 19.8–20.3 during the interval 16 and 17 UT (Figures 2c and 2d), detected the same populations of protons as VAP-A (Figures 3c, 3d, 4d and 4e). After the substorm onset, variations of the flux of the 3–30 keV "nose-structure" proton population were likely related to the radial motion of the ring current with respect to the spacecraft. The innermost plasma sheet/WPC population with energies of tens to hundreds eV appears at ~16:47 UT when the "old" ring current decays.

Similar to VAP-A, the injection seen at VAP-B at ~16:18 UT in the energy range of 50–180 keV exhibits very weak energy-time dispersion in the RBSPICE energy range. The dispersion is masked in HOPE channels by the "nose-structure" protons. The injection at VAP-B is delayed relative to VAP-A. This delay cannot be explained by the proton magnetic drift. For example, the delay for 100 keV proton at $L = 6$ should be 4.5 min keeping in mind 1.5 h of MLT between the two spacecraft. In fact, the delay is only 50 s. This fact and the lack of the significant energy dispersion means that the injection at VAP-B is the result of a shift (or an appearance) of the new injection region, which occupies the VAP-B meridian (ahead of the injected protons drifting from VAP-A). Evidently, this corresponds with the westward expansion of the substorm active region (Figure 2a).

Figure 4f also shows variations of the cold plasma density deduced from EMFISIS wave data. From ~16:20 until 16:47 UT, the density is estimated to be growing from ~150 to ~400 cm$^{-3}$, and it sharply decreases after 16:47 UT. This disappearance of the cold plasma and its replacement for 10–100 eV protons can be interpreted as a joint inward shift of the plasmapause and the innermost plasma sheet. Interestingly, the increase of cold plasma density observed by VAP-B is in antiphase with the behavior of the density at the location of VAP-A, which is only 1.5 h of MLT apart and at lower L-shell. Such formation of the cold plasma undulation longitudinally coinciding with the auroral bulge is in remarkable agreement with observations by Goldstein et al. (2005), which were done during a substrom using the IMAGE spacecraft data.

Figures 3e, 3f, 4g and 4h show the proton data from LEP-i and MEP-i instruments onboard Arase. During the time interval of interest, the Arase spacecraft flew over Scandinavia and Kola Peninsula. At 16 and 17 UT, it was at $L = 5$–5.7 and at MLT = 18.5–19.3, and observed the same proton populations as both VAP spacecraft, except the plasma sheet/WPC intrusion that happened outside this time interval, at ~17:15 UT. The spacecraft started to measure the enhanced proton fluxes at energies less than 80 keV range when it was at $L = 5.37$. The MEP-i detected a short dispersed burst of protons in the range 50–80 keV (at ~16:28 UT) followed by a strong enhancement of the proton flux (at ~16:32 UT) in the 3–80 keV range with leading front exhibiting a clear energy dispersion. The dispersion seen in Figures 4g and 4h means that these particles have been undergone the azimuthal drift. Taking into account the time difference in the arrival of particles of different energies one can determine the location and time of the origin of the abovementioned proton enhancements.
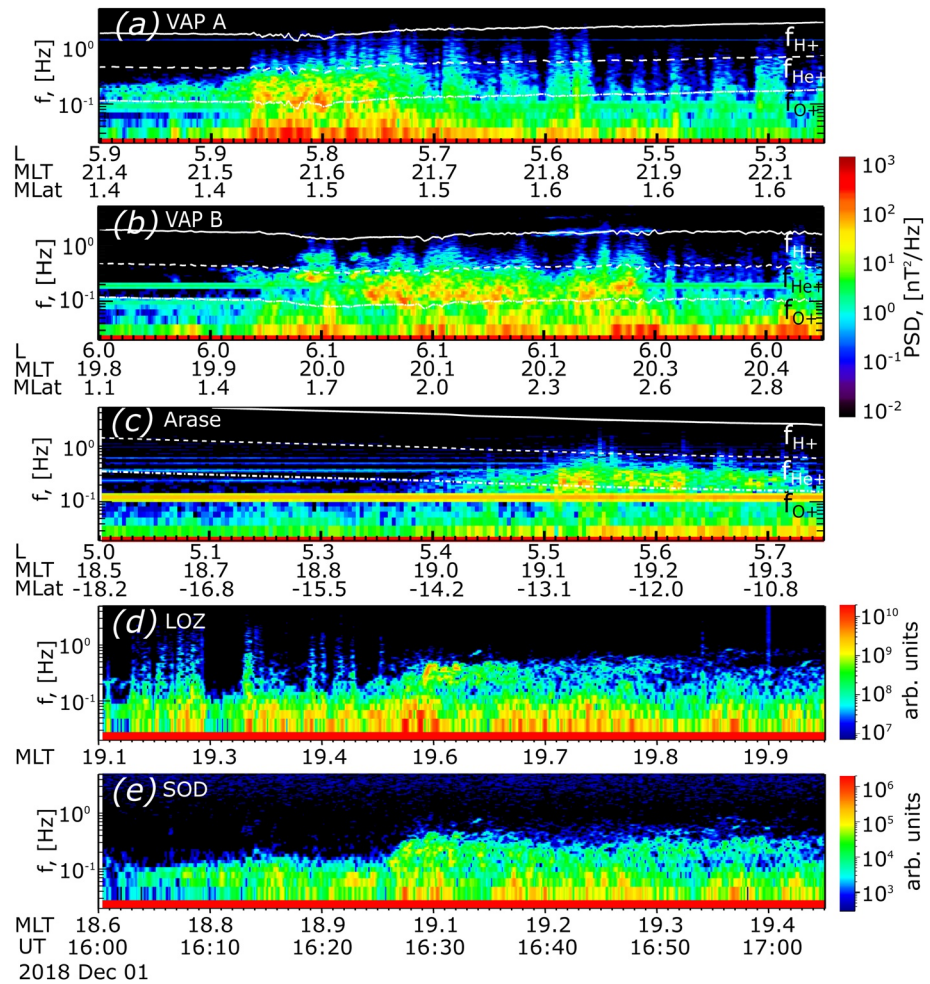
**Figure 5.** Dynamic spectra of magnetic field perpendicular component observed by VAP-A (a), VAP-B (b), and Arase (c) on December 1, 2018. White lines indicate the gyrofrequencies for protons ($f_{H+}$, solid line), helium ($f_{He+}$, dashed line), and oxygen ($f_{O+}$, dash-dotted line). (d, e) Spectrograms of the horizontal magnetic component at Lovozero and Sodankylä.

The backward tracing of protons with energies of ~80 and 60 keV suggests that the first burst was injected at 16:24 UT at ~19.8 MLT. The tracing of protons in the 27–42 keV range shows that the particles forming the front of strong proton flux enhancement were injected at ~16:28 UT at ~19.3 MLT. Thus, both proton enhancements were originated between VAP-B and Arase. This agrees with the location of the westward flank of the substorm region, which, as follows from the auroral and ground magnetometer data, stopped between the meridians of the two spacecraft.

The cold plasma density was calculated based on UHR frequency obtained with the PWE/HFA instrument onboard Arase. It varies around the level of 100 cm$^{-3}$ (Figure 4i) during the interval under consideration until ~17:15 UT when the cold plasma was substituted with the plasma sheet/WPC particles.

### 3.4. EMIC Wave Observations

Figures 5a–5c present spectrograms of magnetic field fluctuations onboard the three spacecraft for the time interval 16:00–17:05 UT. All spacecraft observed the waves in the He+ band at frequencies in the 0.1–0.4 range. VAP-A detected weak EMIC waves seen since 16:00 UT. At 16:13 UT (after the substorm onset), the waves significantly enhanced, and they ended at ~16:26 UT at the same time as the drop in the cold plasma density was detected. VAP-B observed weak EMIC waves at the substorm onset, and they were enhanced

at 16:18 UT. Again, the waves suddenly stopped when cold plasma disappeared at ~16:47 UT. Onboard Arase, the waves were observed from 16:35 to 17:05 UT. The wave activity cessation is not related with the reduction of the cold plasma density that happened 10 min later. The correlation of the EMIC waves and cold plasma density means the observation of the He+ EMIC waves inside the plasmapause. This is in accordance with statistical results by Jun et al. (2019a, 2019b).

The supporting information of this study contains plots (Figures S1– S3) that show characteristics of the waves detected onboard each spacecraft including the parallel component of the Poynting flux, wave normal angle, and ellipticity. For VAP-A and–VAP-B, the wave normal angle is rather small (<20°), the waves are mainly left-hand polarized, and Poynting flux is bi-directional. All these properties imply close location of the spacecraft to the flux tube where the waves were generated (see also Section 4.5). It is not unexpected because, as one can see from Figure 4, the time of wave observations coincided with the arrival of newly injected protons, and the spacecraft were situated near the equatorial plane where the EMIC wave source is typically observed. For Arase, which is rather far from the equatorial plane (MLAT = 10°–15°), the ellipticity is found to be mixed (linear, left-handed, and even right-handed), the wave normal angle is low, and Poynting flux is mainly directed away from the equatorial plane. These features may mean that the spacecraft was within the source flux tube, but out or at the edge of the equatorial source region (see Section 4.5).

Figures 5d and 5e present the spectrograms of geomagnetic pulsations obtained at the Lovozero ($L \approx 5.4$, local MLT midnight is at 20:48 UT) and Sodankylä ($L \approx 5.3$, local MLT midnight is at 21:15 UT) ground-based stations. The pulsations in the range of 0.2–0.5 Hz started with an IPDP-like structure at ~16:28 UT, and continued up to ~17 UT with decreasing intensity and slightly increasing frequency.

### 3.5. Energetic Proton Precipitation Detected by LEO Spacecraft

### 3.5.1. Morphology of the Proton Precipitation

A typical pattern of fluxes of energetic charged particles detected by a low-orbiting satellite crossing mid and high latitudes comprises isotropic fluxes in the poleward part (the isotropic zone) and the fluxes with prevailing transverse anisotropy in the equatorial part (the anisotropic zone) (e.g., Semenova et al., 2019; Yahnin & Yahnina, 2007). The isotropic zone is formed due to the pitch-angle scattering of particles moving through the region where the magnetic field line curvature radius is comparable with the Larmor radius of the particles (e.g., Sergeev & Tsyganenko, 1982) (on the night side it is the equatorial plane of the magnetosphere). The equatorial boundary of such isotropic zone is called the isotropy boundary. Equatorward of this boundary (within the anisotropic zone), the anisotropy can be reduced if another scattering mechanism works. For protons, such mechanism is, most likely, the interaction with EMIC waves. Thus, the emergence of the precipitating protons within the anisotropic zone at low altitudes is often considered as a signature of the ion-cyclotron instability in the magnetosphere (e.g., Yahnin & Yahnina, 2007). The isotropy boundary can sometimes be hidden if the wave-particle interaction zone is juxtaposed with the curvature-scattering zone (Popova et al., 2018).

During the 16 and 17 UT interval, some of POES/MetOp satellites crossed the evening sector, where the westward drifting protons were detected in the magnetosphere. Soon after the substorm onset, at ~16:15–16:17 UT, the MetOp-1 satellite intersected the auroral oval in MLT = ~20.5. Nearly simultaneously, at ~16:16–16:18 UT, MetOp-2 intersected auroras at MLT = ~21.0. Both satellites were between the meridians of VAP-A and VAP-B (MetOp-1 closer to VAP-B, and MetOp-2 closer to VAP-A). Relative locations of the spacecraft are shown in Figure 2c.

Figure 6 (on the left) shows the particle observations during these passes of MetOp-1 and MetOp-2. The data from channels P1–P3 of the MEPED instrument are presented. The proton precipitation patterns at the equatorial edges of both passes look similar to each other. At the poleward edge, a spike of the particle flux is observed by MetOp-2. This is consistent with the auroral bulge signatures seen in Figures 2a and 2b. The isotropic precipitation zones observed by MetOp-1 and MetOp-2 extend equatorward down to $L = 5$–5.3. This might seem inconsistent with the fact that at this time both VAP-A ($L \sim 5.9$) and VAP-B ($L \sim 6$) observe EMIC waves, which require an anisotropic distribution with perpendicular energy exceeding parallel energy for their excitation. We discuss this seeming inconsistency in Section 4.1.
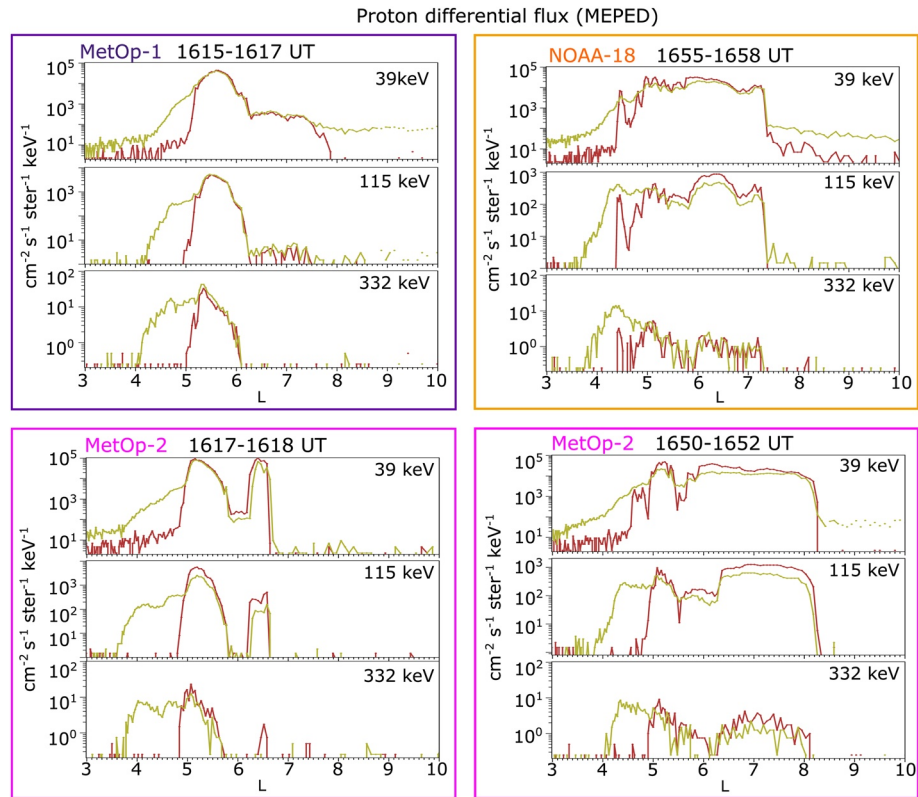
**Figure 6.** Proton fluxes measured in channels P1–P3 of MEPED instrument onboard MetOp-1 at 16:15–16:17 UT (upper left panel), MetOp-2 at 16:17–16:18 UT (bottom left), NOAA-18 at 16:55–16:58 UT (upper right panel), and MetOp-2 at 16:50–16:52 UT (bottom right panel). Red and green lines indicate precipitating and trapped proton flux, respectively.

The proton precipitation patterns observed by MetOp-2 and NOAA-18 at ∼16:51–16:53 and ∼16:55–16:58 UT, respectively, are shown in Figure 6 (on the right). In agreement with the aurora behavior, the POES data show expansion of the precipitation both poleward and equatorward. Some inconsistency between the latitudes of the precipitation and auroras shown in Figure 2 (especially in the poleward parts) can be related to the auroral bulge dynamics during ∼15 min between the auroral and particle observations.

The poleward parts of the proton flux patterns in Figure 6 (right) clearly represent the isotropic zone. At the same time, in this case, it is not easy to determine the location of the isotropy boundary. The anisotropic zone seems to lie below $L \sim 6$. Here, the precipitating flux exhibits rather strong variations; often, it reaches the trapped flux level. This produces multiple regions of the proton flux isotropization, which extend down to $L = 4.4$–$4.6$. In this region, a proton aurora structure is clearly seen equatorward of the substorm electron auroras (see the images for ∼16:40 UT in Figures 2a and 2b).

### 3.6. Spectra of Precipitating Protons

To construct energy spectra of precipitating protons, we used differential flux measurements from four TED and three MEPED proton energy channels. Examples of such spectra for proton precipitation detected by NOAA-18 during flights at 16:55–16:58 UT are shown in Figure 7. The spectra exhibit two precipitating populations. One is characterized by a peak in the range of few to tens of keV, and the other one has energies below 1 keV. The low energy precipitation appears sporadically, and can be related to the WPC population, while the higher-energy precipitated protons could be attributed to the ring current protons scattered by EMIC waves. The latter hypothesis is discussed below.

It is worth noting that proton MEPED telescopes suffer from degradation in time. This leads to some underestimation of the proton flux level (e.g., Asikainen & Mursula, 2011; Sandanger et al., 2015). The
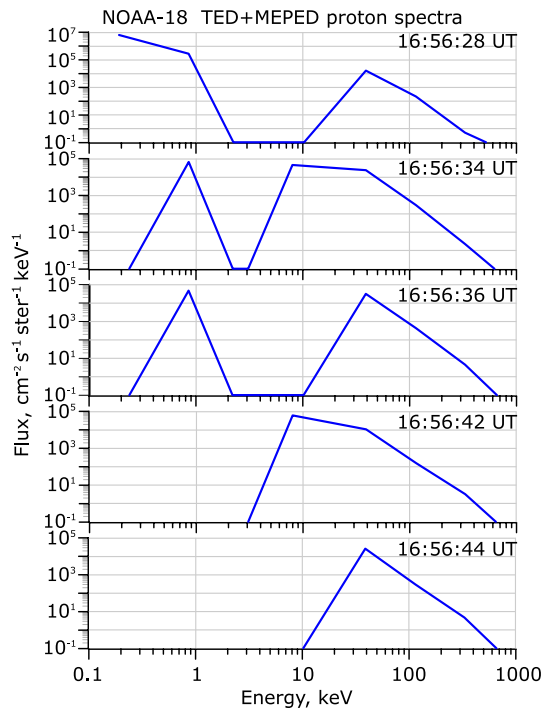
**Figure 7.** Energy spectra of precipitating protons detected by the NOAA-18 satellite at $L = 5$–5.3 during the EMIC wave observations onboard the Arase spacecraft. The times of the spectra are indicated on plots.

underestimation is stronger (up to few times during a decade) in P1 and weaker in P2 and P3. Also, the degradation for 90° telescope is stronger than that for 0° telescope (i.e., why the trapped flux is often slightly lower than precipitating one even in the isotropy zone). Thus, one has to consider the spectra in Figure 7 only as qualitative. It is, nevertheless, clear that an account of degradation will not modify characteristic features of the spectra.

## 4. Discussion

### 4.1. Relationship Between Substorm-Related Proton Enhancements and EMIC Waves

Based on the satellite data, Remya et al. (2018), stressed the role of the injected protons drifting from the substorm region in the generation of the EMIC waves. Similar conclusion has been achieved by using correlations between the ground and satellite data (Søraas et al., 1980; Yahnin et al., 2009). Our consideration shed a light on one more aspect of the relationship between substorms and EMIC wave generation. Namely, our observations suggest that EMIC waves can also be generated within the substorm active region. Indeed, analysis of properties of waves, which were detected by VAP-A and VAP-B situated within the substorm wedge, showed (see Section 3.4 and supporting information) that the observed EMIC waves had low wave normal angles and bi-directional Poynting flux. Such wave properties mean that the observed waves are generated close to the observation point (e.g., Loto'aniu et al., 2005). In addition, westward progression of the EMIC wave region seen on VAP-A and VAP-B was due to westward expansion of the substrom active region, rather than the drift of protons. Later on, when the westward motion of the substorm stopped, the proton cloud drift seen by Arase was the only reason for further westward progression of the EMIC wave region.

During this substorm, the interaction of ring current protons with EMIC waves produces particle precipitation seen by the low-orbiting satellites in a rather wide L-shell range (Section 3.5.1). We relate this with the inward propagation of the substorm injection and related dipolarization of the magnetic field within the substorm wedge (Sergeev et al., 2010). The injection can lead to an increase in the proton flux, and the dipolarization causes a magnetic field enhancement near the equatorial plane and, hence, increases the proton temperature anisotropy. Both these factors favor the generation of the EMIC waves and proton precipitation. (While the injection signatures are clearly seen in Figures 3 and 4, the dipolarization, that is, an increase of the vertical component of the magnetic field is indeed observed by VAP-A after 16:20 UT (Figure 3c) when this spacecraft is well within the substorm wedge. VAP-B situated at the flank of the substorm area sees only weak dipolarization signatures (Figure 3f), and Arase does not see them at all (Figure 3i). Such a magnetic field response is consistent with that expected from the substorm current wedge formation and development (Kepko et al., 2015; McPherron et al., 1973). During the event, by ~16:50 UT, the injection/dipolarization propagated inward to $L = $~4.5, as evidenced by NOAA-18 and MetOp-1 observations of precipitating proton flux (Figure 6).

Interestingly, precipitating flux within the anisotropy zone is often comparable with the trapped one in a wide latitudinal range. This indicates strong pitch-angle diffusion into the loss cone. At the same time, the strong diffusion is evidenced by the diffusion coefficient calculations in section 4.4. We suggest that strong diffusion took place also during MetOp-1 and MetOp-2 flights at 16:17-16:18 UT (Section 3.5.1, Figure 6 (left)). This assumption allows us to resolve the seeming inconsistency (mentioned in Section 3.5.1) between the proton flux isotropy down to $L \sim 5$–5.3 and EMIC waves observed in the magnetosphere at $L \sim 6$. In this case, the zone of proton flux isotropization due to EMIC waves could be juxtaposed with the isotropy boundary, which true location is at $L \geq 6$.

In this event, the background, on which the substorm injections develop, significantly differs from the pure isolated event considered by Remya et al. (2018). In fact, the preceding geomagnetic activity leads to the formation of the enhanced ring population in the form of an "enhanced nose structure" (Ganushkina et al., 2000), which are characterized by rather high proton flux and anisotropy. This population was probably close to marginal stability with respect to the ion-cyclotron instability, and the substorm-related injection only provided additional variations in the flux and anisotropy that triggered the instability. This assumption can explain the fact that some EMIC wave activity was observed by VAP-A and VAP-B earlier than the injection occurred. The latter suggestion is supported by calculations of the EMIC waves growth rate in Section 4.5.

### 4.2. Pc1 Emissions on the Ground and EMIC Waves in Space

One of the puzzling features in the considered event is the lack of observations of the Pc1 emissions on the ground at the time of EMIC wave detection in space. Indeed, due to propagation in the Earth-ionosphere wave-guide, a ground-based station is able to observe Pc1 signal at rather large distance from the ionospheric footprint of the EMIC wave source. Yahnina et al. (2003) found that at the distance of <2 h of MLT almost 100% of localized precipitations of energetic protons, which indicate the field line of the EMIC wave source, were associated with Pc1 or IPDP on the ground. In the considered case, the VAP-B was at a distance of ~1 h of MLT from the ground-based Lovozero and Sodankylä stations. Thus, the signal is expected to be observed at least since 16:18 UT when the EMIC waves appeared at VAP-B. The reason why it is not the case is not quite clear. The fact that similar pulsations were observed at both stations rules out any measurement problems. We may hypothesize, however, that the EMIC waves could not exit to the Earth's surface due to strong disturbances of the ionosphere. When the substorm active region stopped moving (somewhere between VAP-B and Arase), the drifting proton cloud produced EMIC waves outside the disturbed region, and the Pc1 waves started to be observed on the ground (Figures 5d and 5e).

### 4.3. Spatial Extent of the EMIC Wave Source Region

Due to the multipoint EMIC wave observations in space, we can estimate the minimum extent of the region occupied by the waves, which is significant for estimates of their roles in both ring current ion dynamics and relativistic electron precipitation (see also Hendry et al., 2020). In our case, VAP-A and VAP-B observe the EMIC waves simultaneously from 16:15 to 16:30 UT when the distance between them was 1.5 h in MLT. VAP-B and Arase observe the waves simultaneously from 16:35 to 16:48 UT with a distance of 1 h MLT between the spacecraft. Obviously, these values yield only the minimum estimates of the region of simultaneous EMIC wave occurrence. Note that the disappearance of the waves at both VAPs was correlated with a decrease in cold plasma density, and the latter, as evidenced by simultaneous variations in energetic particle fluxes, manifested the inward motion of the plasmasphere with respect to the spacecraft (see Figure 4). Therefore, we may assume that EMIC waves continued to exist at the VAP-A meridian but slightly inward after ~16:30 UT, and the same for the VAP-B meridian after 16:47 UT. In this case, the EMIC wave region could span from the VAP-A to the Arase meridian, that is, to 2.5 h in MLT.

A radial extent of the EMIC wave generation region can be estimated as $1.5\ R_E$ (from $L = 4.5$ to 6) as follows from the low-altitude observations of the energetic proton precipitation (Section 3.5.1) and from the latitudinal width of the proton auroras seen in the ~16:40 UT image in Figure 2b.

### 4.4. Pitch-Angle Diffusion Coefficients and the Diffusion Regime

Using the measured EMIC wave spectra, we calculate the pitch-angle diffusion coefficient $D_{\alpha\alpha}$ of energetic protons near the loss cone. A formula for $D_{\alpha\alpha}$ is well known (see, e.g., Lyons & Williams, 1984; Popova et al., 2020; Summers, 2005).

We use measured local values of the magnetic field and plasma density to calculate the equatorial values. Magnetic field $B$ was calculated by using magnetic latitude according to the dipole model, and the plasma density was assumed to be proportional to $B$. The ion composition for VAP-A and VAP-B was specified according to the particle data in the lowest energy channel of HOPE (~1 eV). The fractions of each ion were
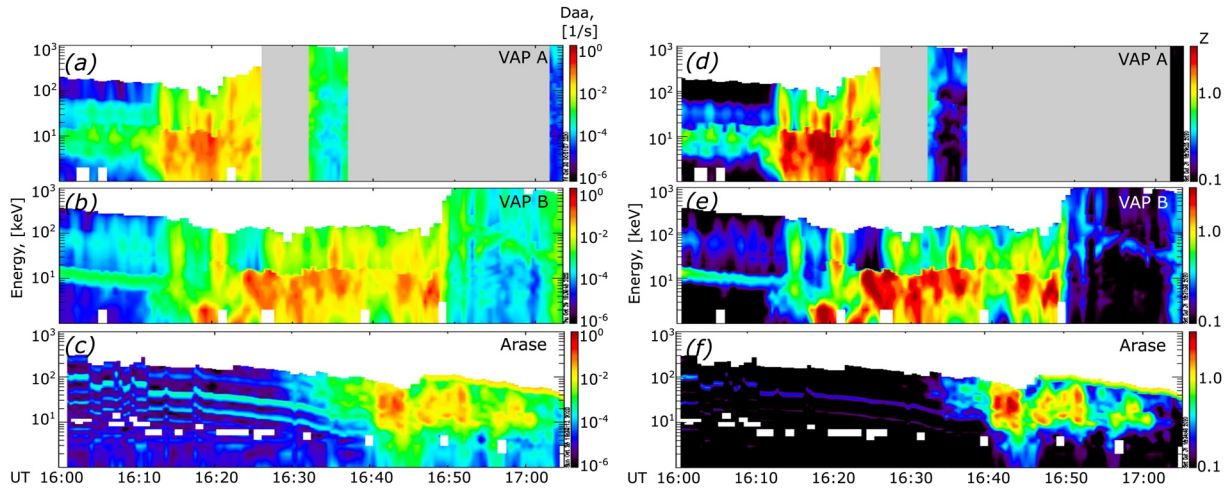
**Figure 8.** Energy spectra of the calculated pitch-angle diffusion coefficient $D_{\alpha\alpha}$ of energetic protons (a)–(c) and the dimensionless parameter $Z$ quantifying the diffusion strength (d–f) for VAP-A (a, d), VAP-B (b, e), and Arase (c, f). Gray regions on panels (a, d) correspond to the absence of cold plasma density data. White areas correspond to the energies at which the resonant interaction is absent.

determined from the available ion omnidirectional flux in this channel. We averaged these values over the interval 16:00–17:00 and obtained the following percentages: 1% O+, 3% He+, 96% p for VAP-A, and 3% O+, 10% He+, 87% p for VAP-B. As for Arase, the LEPi lowest energy channel ($E > 4$ eV) was contaminated, and the next energy channel (30 eV) is too high for the cold component. We decided to use the ion composition for VAP-B also for Arase, since those spacecraft were not far from each other.

Note that we were unable to determine the ion composition from the cutoff frequencies of EMIC waves (e.g., Min et al., 2015; Miyoshi et al., 2019), since the waves are absent above fHe+, and the cutoff and cross-over frequencies are unclear near fO+. The latter fact confirms a low percentage of O+ ions.

The EMIC wave spectral power at the equator was assumed equal to the values measured locally by the spacecraft.

Figures 8a–8c show the diffusion coefficients for the equatorial plane for VAP-A, VAB-B, and Arase, respectively. The plots for local values are qualitatively similar, and the main difference is related to a higher local magnetic field compared to the equatorial one. This yields a shift to lower values of the normalized frequency and, hence, to higher resonance energies. We can see that the energy range of $D_{\alpha\alpha}$ increases at VAP-A on 16:10–16:25 UT and VAP-B on 16:25–16:50 UT is from several keV to 30–50 keV, which corresponds well to the energies of energetic proton ring current population observed at this time (Figure 4). For Arase, an increase in $D_{\alpha\alpha}$ starts around 16:35 UT, and a sharper increase is observed at 16:40 UT for the energy range between 10 and 100 keV. The proton spectrum (Figures 4g and 4h) also shows an increase starting from 16:32 UT, and it becomes sharper at 16:40 UT at 20–30 keV. Since the diffusion coefficient is determined by the EMIC wave spectra, we can infer from its good correspondence to the proton spectra that the waves could be generated by the resonant protons in the flux tubes crossed by the spacecraft. This assumption will be discussed below based on the calculations of the EMIC wave growth rate.

Figures 8d–8f show the dimensionless parameter

$$Z = \left( \overline{D}_{\alpha\alpha} T_b \, / \, \left( 8\mu_c \right) \right)^{1/2}$$

that quantifies the strength of the pitch-angle diffusion (e.g., Trakhtengerts & Rycroft, 2008). Here, $T_b$ is the proton bounce period, and $\mu_c$ is the loss cone boundary ($\mu = \sin^2\theta_{eq}$, where $\theta_{eq}$ is the equatorial pitch-angle). For $Z > 1$, one can expect a strong diffusion (Kennel & Petschek, 1966) with a filled loss cone, while weak diffusion and almost empty loss cone correspond to $Z \ll 1$. For evaluating $Z$, we need to calculate the bounce-averaged pitch-angle diffusion coefficient $\overline{D}_{\alpha\alpha} = T_b^{-1} \int D_{\alpha\alpha} ds \, / \, v_{\parallel}$. This calculation requires a
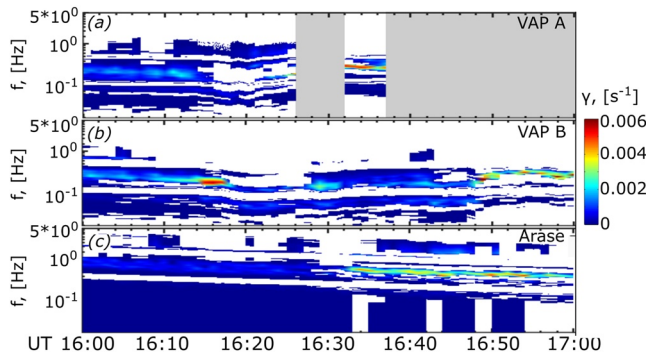
**Figure 9.** Local growth rates $\gamma$ of EMIC waves for VAP-A (a), VAP-B (b), and Arase (c). Only positive values of $\gamma$ are displayed. Gray areas on panels (a) correspond to the absent data on cold plasma density.

knowledge of the distribution all parameters including the wave intensity, plasma density, and magnetic field along the entire flux tube. These unknowns (first of all the wave intensity distribution) impose a high uncertainty in the result of averaging, so it seems sufficient to make only a rough estimate of the averaging effect. The main factor determining this effect is a fraction of the field line where EMIC waves efficiently interact with energetic protons. This region is determined by left-hand polarization and high enough amplitudes of the waves, as well as by a weak nonuniformity of the medium. It is commonly assumed that left-hand EMIC waves occupy a region of magnetic latitudes below about 10°–15° (e.g., Jun et al., 2019b; Loto'aniu et al., 2005; Min et al., 2012; Saikin et al., 2015). In our case, this estimate is supported from below by Arase observations that showed some presence of left-hand EMIC waves at MLAT < 14°. Taking MLAT = 14° as the upper limit of the field-aligned wave distribution, we obtain an averaging factor of 0.2, that has been used in plotting $Z$ in Figures 8d–8f. These plots demonstrate that during the bursts of EMIC waves, the parameter $Z$ exceeds unity, that is, one can expect strong filling of the loss cone. This result agrees with the POES/MetOp observations shown in Figure 6. Indeed, the precipitated fluxes in the maximum are almost equal to the trapped fluxes.

The energy range of the observed enhanced precipitation (10–100 keV) corresponds fairly well to the energy range of enhanced diffusion according to the calculations. This fact indicates that near-equatorial processes provided the main effect of pitch-angle scattering in this event. In the opposite case, one would expect a significant broadening of the diffusion energy range due to the interactions in the off-equatorial regions where the magnetic field is stronger and, hence, the resonance energies are higher.

### 4.5. Calculation of EMIC Wave Growth Rate

To study the possible role of energetic protons in the generation of the EMIC waves detected by the spacecraft, we calculated the growth rate $\gamma$ of these waves by using the procedure described by Lyubchich et al. (2017). This procedure is based on the formula of Kennel and Petschek (1966) and numerical differentiation of the measured energetic proton distribution. We averaged the proton phase space density (PSD) over an interval of 1 min, to decrease the influence of fluctuations. For the ion composition, we used average values for the interval similar to Section 4.4 (1% O+, 3% He+, 96% p for VAP-A, 3% O+, 10% He+, 87% p for VAP-B and Arase).

For VAPs, the local growth rate differs only slightly from the equatorial one, since the spacecraft were close to the equator. The Arase spacecraft was at MLAT of 15°–13°, and using the equatorial values yields a considerable (about 0.2 Hz) decrease in the growth rate frequency range. However, recalculation of the equatorial PSD from the local one may cause errors at pitch angles above 61° that correspond to the particles mirroring above the spacecraft. Therefore, we present only local growth rates. They are shown in Figures 9a–9c. We used only those time intervals for which the plasma density data based on UHR emissions are available. Only positive values of $\gamma$ are displayed.

One clearly sees the gaps of $\gamma$ around the local He+ and O+ gyrofrequencies, and some maxima between these frequencies.

The growth rate for Arase increased at 16:34 UT. That corresponds quite well to the appearance of EMIC waves detected by Arase. The frequency range of the observed EMIC waves agrees in general with that of $\gamma$, although the former is broader and spans to lower frequencies. As it was noted above, the equatorial values of $\gamma$ would correspond better to the observed wave frequencies due to a difference between the equatorial and local magnetic fields.

The situation is different for the intervals of EMIC wave observation by both VAPs. Figures 9a and 9b demonstrate intervals of negative growth rate in the frequency-time domains where the EMIC waves were observed by VAP-A and VAP-B, respectively. For VAP-A, this interval lasts from 16:15 to 16:26 UT, and for

VAP-B, from 16:18 to 16:29 UT. Before the beginning of those intervals, one can see regions of positive but rather low growth rates for both VAP-A and VAP-B (16:00–16:15 UT). Some weaker wave activity in the same frequency range was observed at that time by VAP-A, and it started to increase from 16:12 UT when the calculated growth rate was still positive. For VAP-B, an increase in the growth rate from 16:10 to 16:18 UT was also accompanied by a wave activity in approximately the same frequency range. Then a stronger increase in the wave power corresponded to the interval of negative growth rate. However, the wave activity in the He + band continued also after that time interval (till 16:50 UT, see Figure 5b). During this interval, the growth rate was first positive in the lower-frequency part of the range occupied by the waves (below 0.2 Hz), whereas it was almost zero and then became negative (at 16:45 UT) for the higher frequency part of the He+ range.

When comparing the observed wave spectra and the calculated growth rates, two facts should be taken into account. On the one hand, the wave generation causes the pitch-angle diffusion that drives the distribution function to a marginal stability, that is, zero total growth rate (e.g., Noh et al., 2018; Saikin et al., 2018; Trakhtengerts & Rycroft, 2008; Williams & Lyons, 1974). On the other hand, the waves can only persist for sufficiently long time until they continue gaining energy from some source, since there are always losses due to refraction and incomplete reflection. The wave one-hop time is several tens of seconds for EMIC waves, that is, the wave observed during 10–20 min certainly requires a persistent energy supply. If this supply is due to the wave growth in the same flux tube, then the growth rate should remain positive in this flux tube. An alternative energy source can be their transfer from neighboring flux tubes. In the latter case, the growth rate does not need to be positive in the region of wave observation.

Given the above, the negative growth rate during the EMIC wave observation by VAP-A and VAP-B implies that the spacecraft were outside the flux tube where the waves were generated during the corresponding time intervals. Transitions from negative to positive growth rate and back obtained for VAP-B could mean that the spacecraft was in a close vicinity of the generation flux tube, and eventually may have crossed it. Similarly, based on more prolonged interval of positive growth rate obtained for Arase, we may assume that Arase was crossing the flux tube where the observed EMIC waves were generated.

## 5. Conclusions

We described the observations made by three spacecraft (VAPs A and B and Arase) during a substorm in the evening-night sector in the vicinity of the equatorial plane of the near-Earth magnetosphere. The spacecraft were located at close L-shells ($L = 5.5–6$) but were separated in MLT by 1.5–2.5 h, and observed substorm proton injections within the substorm wedge and drifting proton cloud outside of the substorm active region. In all cases, the spacecraft detected enhancement or appearance of the EMIC waves. To our knowledge, this is the first direct evidence of the fact that the EMIC waves can be generated well inside the area of the substorm development. The necessary conditions for EMIC wave generation could be created due to proton injection and related dipolarization which enhance the proton flux and proton temperature anisotropy within the substorm area.

Several passes of low-orbiting NOAA POES and MetOp satellites revealed proton precipitation in the 1–100 keV energy range due to the EMIC wave- proton interaction within the anisotropic zone.

Based on the longitudinally separated spacecraft measurements of EMIC waves and the low-orbiting satellite observations of the EMIC wave-driven proton precipitation, we could estimate the lower limit for the EMIC wave generation area as ∼2 h of MLT and 1.5 Re in the radial direction.

Interestingly, there was no Pc1 signal detected on the ground while the EMIC wave generation was inside the substorm area. This could be related to the impossibility of wave exit to the ground through the disturbed ionosphere. Pc1 pulsations started to be detected on the ground when the substorm westward progression stopped, and further movement of the EMIC wave source was due to proton cloud westward drift.

We concluded that the EMIC-related precipitating proton flux observed at low-altitude was comparable with the trapped flux. This means a strong diffusion process, and this was confirmed by our calculations of the diffusion coefficient and strong diffusion index, which are based on the observed wave, plasma, and

magnetic field parameters. The diffusion coefficient maximum corresponded well to the energy range of the observed proton precipitation.

The growth rate calculations based on the plasma and magnetic field data from both VAP and Arase spacecraft indicated that the detected EMIC waves could be generated in the region of their observation or in its close vicinity. The growth rate was negative in the region where intense waves were observed by both VAPs. This fact can be explained by a decrease in the proton pitch-angle anisotropy due to the pitch-angle diffusion by the EMIC waves. In this case, the result implies an assumption that the observed waves were generated in a region neighbor to the spacecraft.

Our results demonstrate a great potential of multi-point observations of near-Earth space phenomena by several spacecraft located in the magnetosphere and at low orbits. The era of simultaneous operation of the VAPs and Arase spacecraft provides an opportunity for new steps in this direction.

## Data Availability Statement

Van Allen Probe data used in this study can be found in the EMFISIS (https://emfisis.physics.uiowa.edu/data/index), and RBSP-ECT (https://www.RBSP-ect.lanl.gov/) archives. Science data of the Arase (ERG) satellite were obtained from the ERG Science Center operated by ISAS/JAXA and ISEE/Nagoya University (https://ergsc.isee.nagoya-u.ac.jp/index.shtml.en, Miyoshi, Hori, et al., 2018). The present study analyzed MGF-L2 v03_04 data (Matsuoka, Teramoto, Imajo, et al., 2018), EFD/PWE-L2 v01 (Kasahara et al., 2020), LEP-i-L2 3D flux v03_00 data (Asamura, Miyoshi, et al., 2018), MEP-i-L2 3D flux v01_02 data (Yokota et al., 2019), and Orbit L3 v01 data (Miyoshi, Shinohara, & Jun, 2018).

## References

Akasofu, S. I. (1977). *Physics of magnetospheric substorms*. D. Reidel. https://doi.org/10.1007/978-94-010-1164-8

Alken, P., Thébault, E., Beggan, C. D., Amit, H., Aubert, J., Baerenzung, J., et al. (2021). International geomagnetic reference field: The thirteenth generation. *Earth, Planets and Space*, *73*, 49. https://doi.org/10.1186/s40623-020-01288-x

Allen, R. C., Zhang, J.-C., Kistler, L. M., Spence, H. E., Lin, R.-L., Klecker, B., et al. (2016). A statistical study of EMIC waves observed by Cluster: 2. Associated plasma conditions. *Journal of Geophysical Research: Space Physics*, *121*, 6458–6479. https://doi.org/10.1002/2016JA022541

Asamura, K., Kazama, Y., Yokota, S., Kasahara, S., & Miyoshi, Y. (2018). Low-energy particle experiments–ion mass analyzer (LEPi) onboard the ERG (Arase) satellite. *Earth, Planets and Space*, *70*, 70. https://doi.org/10.1186/s40623-018-0846-0

Asamura, K., Miyoshi, Y., & Shinohara, I. (2018). The LEPi instrument Level-2 3D flux data of Exploration of energization and Radiation in Geospace (ERG) Arase satellite. 10 01.Version v03_00, updated daily, ERG Science Center AXA. Institute for Space-Earth Environmental Research, Nagoya University. https://doi.org/10.34515/DATA.ERG-05000

Asikainen, T., & Mursula, K. (2011). Recalibration of the long-term NOAA/MEPED energetic proton measurements. *Journal of Atmospheric and Solar-Terrestrial Physics*, *73*(2–3), 335–347. https://doi.org/10.1016/j.jastp.2009.12.011

Beletskii, A. B., Rakhmatulin, R. A., Syrenova, T. Y., Vasilev, R. V., Mikhalev, A. V., Pashinin, A. Y., et al. (2019). Preliminary results of simultaneous recording of auroral and geomagnetic pulsations at the ISTP SB RAS station Istok. *Solar-Terrestrial Physics*, *5*(2), 39–44. https://doi.org/10.12737/stp-52201906

Bespalov, P. A., Grafe, A., Demekhov, A. G., & Trakhtengerts, V. Y. (1994). On the role of collective interactions in asymmetric ring current formation. *Annales Geophysicae*, *12*(5), 422–430. https://doi.org/10.1007/s00585-994-0422-8

Birn, J., Hesse, M., Nakamura, R., & Zaharia, S. (2013). Particle acceleration in dipolarization events. *Journal of Geophysical Research: Space Physics*, *118*, 1960–1971. https://doi.org/10.1002/jgra.50132

Birn, J., Thomsen, M. F., Borovsky, J. E., Reeves, G. D., McComas, D. J., & Belian, R. D. (1997). Characteristic plasma properties during dispersionless substorm injections at geosynchronous orbit. *Journal of Geophysical Research*, *102*(A2), 2309–2324. https://doi.org/10.1029/96JA02870

Chappell, C. R., Huddleston, M. M., Moore, T. E., Giles, B. L., & Delcourt, D. C. (2008). Observations of the warm plasma cloak and an explanation of its formation in the magnetosphere. *Journal of Geophysical Research*, *113*, A09206. https://doi.org/10.1029/2007JA012945

Chen, H., Gao, X., Lu, Q., Tsurutani, B. T., & Wang, S. (2020). Statistical evidence for EMIC wave excitation driven by substorm injection and enhanced solar wind pressure in the Earth's magnetosphere: Two different EMIC wave sources. *Geophysical Research Letters*, *47*, e2020GL090275. https://doi.org/10.1029/2020GL090275

Cornwall, J. M., Coroniti, F. V., & Thorne, R. M. (1970). Turbulent loss of ring current protons. *Journal of Geophysical Research*, *75*(25), 4699–4709. https://doi.org/10.1029/JA075i025p04699

DeForest, S. E., & McIlwain, C. E. (1971). Plasma clouds in the magnetosphere. *Journal of Geophysical Research*, *76*(16), 3587–3611. https://doi.org/10.1029/JA076i016p03587

Engebretson, M. J., Posch, J. L., Wygant, J. R., Kletzing, C. A., Lessard, M. R., Huang, C.-L., et al. (2015). Van Allen probes, NOAA, GOES, and ground observations of an intense EMIC wave event extending over 12 h in magnetic local time. *Journal of Geophysical Research: Space Physics*, *120*, 5465–5488. https://doi.org/10.1002/2015JA021227

Evans, D. S., & Greer, M. S. (2004). Polar orbiting environmental satellite space experiment monitor-2: Instrument descriptions and archive data documentation. NOAA Technical Memorandum Version 1.3. NOAA Space Environment Center.

Fairfield, D. H., & Viñas, A. F. (1984). The inner edge of the plasma sheet and the diffuse aurora. *Journal of Geophysical Research*, *89*(A2), 841–854. https://doi.org/10.1029/JA089iA02p00841

Feldstein, Y. I., & Galperin, Y. I. (1985). The auroral luminosity structure in the high-latitude upper atmosphere: Its dynamics and relationship to the large-scale structure of the Earth's magnetosphere. *Reviews of Geophysics*, *23*(3), 217–275. https://doi.org/10.1029/RG023i003p00217

Funsten, H. O., Skoug, R. M., Guthrie, A. A., MacDonald, E. A., Baldonado, J. R., Harper, R. W., et al. (2013). Helium, Oxygen, Proton, and Electron (HOPE) mass spectrometer for the radiation belt storm probes mission. *Space Science Reviews*, *179*, 423–484. https://doi.org/10.1007/s11214-013-9968-7

Ganushkina, N. Y., Pulkkinen, T. I., Sergeev, V. A., Kubyshkina, M. V., Baker, D. N., Turner, N. E., et al. (2000). Entry of plasma sheet particles into the inner magnetosphere as observed by Polar/CAMMICE. *Journal of Geophysical Research*, *105*(A11), 25205–25219. https://doi.org/10.1029/2000JA900062

Gary, S. P., Moldwin, M. B., Thomsen, M. F., Winske, D., & McComas, D. J. (1994). Hot proton anisotropies and cool proton temperatures in the outer magnetosphere. *Journal of Geophysical Research*, *99*(A12), 23603. https://doi.org/10.1029/94ja02069

Gjerloev, J. W. (2012). The SuperMAG data processing technique. *Journal of Geophysical Research*, *117*, A09213. https://doi.org/10.1029/2012JA017683

Goldstein, J., Burch, J. L., Sandel, B. R., Mende, S. B., C son Brandt, P., & Hairston, M. R. (2005). Coupled response of the inner magnetosphere and ionosphere on 17 April 2002. *Journal of Geophysical Research*, *110*, A03205. https://doi.org/10.1029/2004JA010712

Halford, A. J., Fraser, B. J., & Morley, S. K. (2010). EMIC wave activity during geomagnetic storm and nonstorm periods: CRRES results. *Journal of Geophysical Research: Space Physics*, *115*, A12248–A12263. https://doi.org/10.1029/2010JA015716

Halford, A. J., Fraser, B. J., Morley, S. K., Elkington, S. R., & Chan, A. A. (2016). Dependence of EMIC wave parameters during quiet, geomagnetic storm, and geomagnetic storm phase times. *Journal of Geophysical Research: Space Physics*, *121*, 6277–6291. https://doi.org/10.1002/2016JA022694

Hendry, A. T., Santolik, O., Miyoshi, Y., Matsuoka, A., Rodger, C. J., Clilverd, M. A., et al. (2020). A multi-instrument approach to determining the source-region extent of EEP-driving EMIC waves. *Geophysical Research Letters*, *47*, e2019GL086599. https://doi.org/10.1029/2019GL086599

Jordanova, V. K., Albert, J., & Miyoshi, Y. (2008). Relativistic electron precipitation by EMIC waves from self-consistent global simulations. *Journal of Geophysical Research: Space Physics*, *113*, A00A10–A00A21. https://doi.org/10.1029/2008JA013239

Jordanova, V. K., Farrugia, C. J., Thorne, R. M., Khazanov, G. V., Reeves, G. D., & Thomsen, M. F. (2001). Modeling ring current proton precipitation by electromagnetic ion cyclotron waves during the May 14–16, 1997, storm. *Journal of Geophysical Research*, *106*, 7–22. https://doi.org/10.1029/2000JA002008

Jun, C.-W., Yue, C., Bortnik, J., Lyons, L. R., Nishimura, Y. T., Kletzing, C. A., et al. (2019a). A statistical study of EMIC waves associated with and without energetic particle injection from the magnetotail. *Journal of Geophysical Research: Space Physics*, *124*, 433–450. https://doi.org/10.1029/2018JA025886

Jun, C.-W., Yue, C., Bortnik, J., Lyons, L. R., Nishimura, Y. T., & Kletzing, C. A. (2019b). EMIC wave properties associated with and without injections in the inner magnetosphere. *Journal of Geophysical Research: Space Physics*, *124*, 2029–2045. https://doi.org/10.1029/2018JA026279

Kangas, J., Guglielmi, A., & Pokhotelov, O. (1998). Morphology and physics of short-period magnetic pulsations (a review). *Space Science Reviews*, *83*, 435–512. https://doi.org/10.1023/a:1005063911643

Kasaba, Y., Ishisaka, K., Kasahara, Y., Imachi, T., Yagitani, S., Kojima, H., et al. (2017). Wire Probe Antenna (WPT) and Electric Field Detector (EFD) of Plasma Wave Experiment (PWE) aboard the Arase satellite: Specifications and initial evaluation results. *Earth, Planets and Space*, *69*, 174. https://doi.org/10.1186/s40623-017-0760-x

Kasahara, Y., Kasaba, Y., Kojima, H., Yagitani, S., Ishisaka, K., Kumamoto, A., et al. (2018). The Plasma Wave Experiment (PWE) on board the Arase (ERG) satellite. *Earth, Planets and Space*, *70*, 86. https://doi.org/10.1186/s40623-018-0842-4

Kasahara, Y., Kasaba, Y., Matsuda, S., Shoji, M., Nakgawa, T., Ishisaka, K., et al. (2020). *The PWE/EFD instrument Level-2 electric field waveform data of Exploration of energization and Radiation in Geospace (ERG) Arase satellite*. https://doi.org/10.34515/DATA.ERG-07003

Kasahara, Y., Kumamoto, A., Tsuchiya, F., Matsuda, S., Shoji, M., Nakamura, S., et al. (2018). *The PWE/HFA instrument Level-2 spectrum data of Exploration of energization and Radiation in Geospace (ERG) Arase satellite*. https://doi.org/10.34515/DATA.ERG-10000

Keika, K., Takahashi, K., Ukhorskiy, A. Y., & Miyoshi, Y. (2013). Global characteristics of electromagnetic ion cyclotron waves: Occurrence rate and its storm dependence. *Journal of Geophysical Research: Space Physics*, *118*, 4135–4150. https://doi.org/10.1002/jgra.50385

Kennel, C. F., & Petschek, H. E. (1966). Limit of stably trapped particle fluxes. *Journal of Geophysical Research*, *71*(1), 1–28. https://doi.org/10.1029/jz071i001p00001

Kepko, L., McPherron, R. L., Amm, O., Apatenkov, S., Baumjohann, W., Birn, J., et al. (2015). Substorm current wedge revisited. *Space Science Reviews*, *190*, 1–46. https://doi.org/10.1007/s11214-014-0124-9

Kim, H., Schiller, Q., Engebretson, M. J., Noh, S., Kuzichev, I., Lanzerotti, L. J., et al. (2021). Observations of particle loss due to injection-associated electromagnetic ion cyclotron waves. *Journal of Geophysical Research: Space Physics*, *126*, e2020JA028503. https://doi.org/10.1029/2020JA028503

Kletzing, C. A., Kurth, W. S., Acuna, M., MacDowall, R. J., Torbert, R. B., Averkamp, T., et al. (2013). The Electric and Magnetic Field Instrument Suite and Integrated Science (EMFISIS) on RBSP. *Space Science Reviews*, *179*, 127–181. https://doi.org/10.1007/s11214-013-9993-6

Kozyra, J. U., Cravens, T. E., Nagy, A. F., Fontheim, E. G., & Ong, R. S. B. (1984). Effects of energetic heavy ions on electromagnetic ion cyclotron wave generation in the plasmapause region. *Journal of Geophysical Research*, *89*(A4), 2217. https://doi.org/10.1029/ja089ia04p02217

Kumamoto, A., Tsuchiya, F., Kasahara, Y., Kasaba, Y., Kojima, H., Yagitani, S., et al. (2018). High Frequency Analyzer (HFA) of Plasma Wave Experiment (PWE) onboard the Arase spacecraft. *Earth, Planets and Space*, *70*, 82. https://doi.org/10.1186/s40623-018-0854-0

Loto'aniu, T. M., Fraser, B. J., & Waters, C. L. (2005). Propagation of electromagnetic ion cyclotron wave energy in the magnetosphere. *Journal of Geophysical Research: Space Physics*, *110*, A07214–A07224. https://doi.org/10.1029/2004JA010816

Lubchich, A. A., & Semenova, N. V. (2015). Modeling of the electromagnetic ion cyclotron wave generation in the H+-HE+ plasma of the inner magnetosphere. *Journal of Atmospheric and Solar-Terrestrial Physics*, *125–126*, 21–37. https://doi.org/10.1016/j.jastp.2015.02.004

Lyons, L. R., & Williams, D. J. (1984). *Quantitative aspects of magnetospheric physics*. D. Reidel.

Lyubchich, A. A., Demekhov, A. G., Titova, E. E., & Yahnin, A. G. (2017). Amplitude-frequency characteristics of ion-cyclotron and whistler-mode waves from Van Allen Probes data. *Geomagnetism and Aeronomy*, *57*(1), 40–50. https://doi.org/10.1134/S001679321701008X

Matsuda, S., Kasahara, Y., Miyoshi, Y., Nomura, R., Shoji, M., Matsuoka, A., et al. (2018). Spatial distribution of fine-structured and unstructured EMIC waves observed by the Arase satellite. *Geophysical Research Letters*, *45*, 11530–11538. https://doi.org/10.1029/2018GL080109

Matsuoka, A., Teramoto, M., Imajo, S., Kurita, S., Miyoshi, Y., & Shinohara, I. (2018). *The MGF instrument Level-2 spin-fit magnetic field data of Exploration of energization and Radiation in Geospace (ERG) Arase satellite, Version v03.03, updated daily*, ERG Science Center, Institute for Space-Earth Environmental Research. https://doi.org/10.34515/DATA.ERG-06001

Matsuoka, A., Teramoto, M., Nomura, R., Nosé, M., Fujimoto, A., Tanaka, Y., et al. (2018). The ARASE (ERG) magnetic field investigation. *Earth, Planets and Space*, *70*, 43. https://doi.org/10.1186/s40623-018-0800-1

Mauk, B. H., Fox, N. J., Kanekal, S. G., Kessel, R. L., Sibeck, D. G., & Ukhorskiy, A. (2013). Science objectives and rationale for the radiation belt storm probes mission. *Space Science Reviews*, *179*, 3–27. https://doi.org/10.1007/s11214-012-9908-y

McCollough, J. P., Elkington, S. R., Usanova, M. E., Mann, I. R., Baker, D. N., & Kale, Z. C. (2010). Physical mechanisms of compressional EMIC wave growth. *Journal of Geophysical Research*, *115*, A10214. https://doi.org/10.1029/2010JA015393

McPherron, R. L., Russell, C. T., & Aubry, M. (1973). Satellite studies of magnetospheric substorms on August 15, 1968, 9. Phenomenological model for substorms. *Journal of Geophysical Research*, *78*(16), 3131–3149. https://doi.org/10.1029/ja078i016p03131

Meredith, N. P., Horne, R. B., Kersten, T., Fraser, B. J., & Grew, R. S. (2014). Global morphology and spectral properties of EMIC waves derived from CRRES observations. *Journal of Geophysical Research*, *119*, 5328–5342. https://doi.org/10.1002/2014JA020064

Min, K., Lee, J., Keika, K., & Li, W. (2012). Global distribution of EMIC waves derived from THEMIS observations. *Journal of Geophysical Research*, *117*, A05219. https://doi.org/10.1029/2012JA017515

Min, K., Liu, K., Bonnell, J. W., Breneman, A. W., Denton, R. E., Funsten, H. O., et al. (2015). Study of EMIC wave excitation using direct ion measurements. *Journal of Geophysical Research: Space Physics*, *120*(4), 2702–2719. https://doi.org/10.1002/2014JA020717

Mitchell, D. G., Lanzerotti, L. J., Kim, C. K., Stokes, M., Ho, G., Cooper, S., et al. (2013). Radiation Belt Storm Probes Ion Composition Experiment (RBSPICE). *Space Science Reviews*, *179*, 263–308. https://doi.org/10.1007/s11214-013-9965-x

Miyoshi, Y., Hori, T., Shoji, M., Teramoto, M., Chang, T. F., Segawa, T., et al. (2018). The ERG science center. *Earth, Planets and Space*, *70*, 96. https://doi.org/10.1186/s40623-018-0867-8

Miyoshi, Y., Matsuda, S., Kurita, S., Nomura, K., Keika, K., Shoji, M., et al. (2019). EMIC waves converted from equatorial noise due to M/Q = 2 ions in the plasmasphere: Observations from Van Allen Probes and Arase. *Geophysical Research Letters*, *46*, 5662–5669. https://doi.org/10.1029/2019GL083024

Miyoshi, Y., Sakaguchi, K., Shiokawa, K., Evans, D., Albert, J., Conners, M., & Jordanova, V. (2008). Precipitation of radiation belt electrons by EMIC waves, observed from ground and space. *Geophysical Research Letters*, *35*, L23101. https://doi.org/10.1029/2008GL035727

Miyoshi, Y., Shinohara, I., & Jun, C.-W. (2018). *The Level-3 orbit data of Exploration of energization and Radiation in Geospace (ERG) Arase satellite, TS04 model. Version v01_00, updated daily*. ERG Science Center, Institute for Space-Earth Environmental Research, Nagoya University. https://doi.org/10.34515/DATA.ERG-12001

Miyoshi, Y., Shinohara, I., Takashima, T., Asamura, K., Higashio, N., Mitani, T., et al. (2018). Geospace exploration project ERG. *Earth, Planets and Space*, *70*, 101. https://doi.org/10.1186/s40623-018-0862-0

Newell, P. T., & Gjerloev, J. W. (2011). Evaluation of SuperMAG auroral electrojet indices as indicators of substorms and auroral power. *Journal of Geophysical Research*, *116*, A12211. https://doi.org/10.1029/2011JA016779

Newell, P. T., & Gjerloev, J. W. (2012). SuperMAG-based partial ring current indices. *Journal of Geophysical Research*, *117*. https://doi.org/10.1029/2012JA017586

Noh, S.-J., Lee, D.-Y., Choi, C.-R., Kim, H., & Skoug, R. (2018). Test of ion cyclotron resonance instability using proton distributions obtained from Van Allen Probe—A observations. *Journal of Geophysical Research: Space Physics*, *123*(8), 6591–6610. https://doi.org/10.1029/2018ja025385

Olson, J. V., & Lee, L. C. (1983). Pc1 wave generation by sudden impulses. *Planetary and Space Science*, *31*, 295–302. https://doi.org/10.1016/0032-0633(83)90079-x

Paxton, L., Morrison, D., Zhang, Y., Kil, H., Wolven, B., Ogorzalek, B. S., et al. (2002). Validation of remote sensing products produced by the Special Sensor Ultraviolet Scanning Imager (SSUSI): A far UV-imaging spectrograph on DMSP F-16, *Proceedings of the SPIE 4485, Optical Spectroscopic Techniques, Remote Sensing, and Instrumentation for Atmospheric and Space Research IV*. https://doi.org/10.1117/12.454268

Popova, T. A., Lyubchich, A., Demekhov, A., & Yahnin, A. (2020). Pitch-angle diffusion of energetic protons upon their interaction with EMIC waves: Comparison of calculation results with THEMIS and NOAA/POES data. In T. Yanovskaya, A. Kosterov, N. Bobrov, A. Divin, A. Saraev, & N. Zolotova (Eds.), *Problems of Geocosmos–2018, Springer Proceedings in Earth and Environmental Sciences*. Springer. https://doi.org/10.1007/978-3-030-21788-4_27

Popova, T. A., Yahnin, A. G., Demekhov, A. G., & Chernyaeva, S. A. (2018). Generation of EMIC waves in the magnetosphere and precipitation of energetic protons: Comparison of the data from THEMIS high earth orbiting satellites and POES low earth orbiting satellites. *Geomagnetism and Aeronomy*, *58*, 469–482. https://doi.org/10.1134/S0016793218040114

Popova, T. A., Yahnin, A. G., Yahnina, T. A., & Frey, H. (2010). Relation between sudden increases in the solar wind dynamic pressure, auroral proton flashes, and geomagnetic pulsations in the Pc1 range. *Geomagnetism and Aeronomy*, *50*, 568–575. https://doi.org/10.1134/S0016793210050038

Reeves, G. D. (1998). New perspectives on substorm injections. In S. Kokubun, & Y. Kamide (Eds.), *Substorms 4: Proceedings of ICS-4* (p. 785). Kluwer Academy. https://doi.org/10.1007/978-94-011-4798-9_163

Reeves, G. D., Belian, R. D., & Fritz, T. A. (1991). Numerical tracing of energetic particle drifts in a model magnetosphere. *Journal of Geophysical Research: Space Physics*, *96*(A8), 13997–14008. https://doi.org/10.1029/91ja01161

Remya, B., Sibeck, D. G., Halford, A. J., Murphy, K. R., Reeves, G. D., Singer, H. J., et al. (2018). Ion injection triggered EMIC waves in the Earth's magnetosphere. *Journal of Geophysical Research: Space Physics*, *123*. https://doi.org/10.1029/2018JA025354

Remya, B., Sibeck, D. G., Halford, A. J., Murphy, K. R., Reeves, G. D., Singer, H. J., et al. (2019). *Statistical distribution of EMIC waves and dependence on substorm injections* (pp. 9–15). URSI AP-RASC 2019.

Rodger, C. J., Carson, B. R., Cummer, S. A., Gamble, R. J., Clilverd, M. A., Green, J. C., et al. (2010). Contrasting the efficiency of radiation belt losses caused by ducted and nonducted whistler mode waves from ground-based transmitters. *Journal of Geophysical Research*, *115*, A12208. https://doi.org/10.1029/2010JA015880

Rodger, C. J., Clilverd, M. A., Green, J. C., & Lam, M. M. (2010). Use of POES SEM-2 observations to examine radiation belt dynamics and energetic electron precipitation into the atmosphere. *Journal of Geophysical Research*, *115*, A04202. https://doi.org/10.1029/2008JA014023

Rostoker, G., Akasofu, S.-I., Foster, J., Greenwald, R., Kamide, Y., Kawasaki, K., et al. (1980). Magnetospheric substorms—Definition and signatures. *Journal of Geophysical Research*, *85*(A4), 1663–1668. https://doi.org/10.1029/JA085iA04p01663

Sagdeev, R. Z., & Shafranov, V. D. (1961). On the instability of a plasma with an anisotropic distribution of velocity in a mangetic filed. *Soviet Physics, JETP*, *12*, 130–132.

Saikin, A. A., Jordanova, V. K., Zhang, J.-C., Smith, C. W., Spence, H. E., Larsen, B. A., et al. (2018). Comparing simulated and observed EMIC wave amplitudes using in situ Van Allen Probes' measurements. *Journal of Atmospheric and Solar-Terrestrial Physics*, *177*, 190–201. https://doi.org/10.1016/j.jastp.2018.01.024

Saikin, A. A., Zhang, J.-C., Allen, R. C., Smith, C. W., Kistler, L. M., Spence, H. E., et al. (2015). The occurrence and wave properties of H+-, He+-, and O+-band EMIC waves observed by the Van Allen Probes. *Journal of Geophysical Research: Space Physics*, *120*, 1–16. https://doi.org/10.1002/2015JA021358

Saikin, A. A., Zhang, J.-C., Smith, C. W., Spence, H. E., Torbert, R. B., & Kletzing, C. A. (2016). The dependence on geomagnetic conditions and solar wind dynamic pressure of the spatial distributions of EMIC waves observed by the Van Allen Probes. *Journal of Geophysical Research: Space Physics*, *121*, 4362–4377. https://doi.org/10.1002/2016JA02260610.1002/2016ja022523

Sandanger, M. I., Ødegaard, L.-K. G., Nesse Tyssøy, H., Stadsnes, J., Søraas, F., Oksavik, K., & Aarsnes, K. (2015). In-flight calibration of NOAA POES proton detectors—Derivation of the MEPED correction factors. *Journal of Geophysical Research: Space Physics*, *120*, 9578–9593. https://doi.org/10.1002/2015JA021388

Semenova, N. V., Yahnin, A. G., Yahnina, T. A., & Demekhov, A. G. (2019). Properties of localized precipitation of energetic protons equatorward of the isotropic boundary. *Geophysical Research Letters*, *46*, 10932–10940. https://doi.org/10.1029/2019gl085373

Sergeev, V. A., Kornilova, T. A., Kornilov, I. A., Angelopoulos, V., Kubyshkina, M. V., Fillingim, M., et al. (2010). Auroral signatures of the plasma injection and dipolarization in the inner magnetosphere. *Journal of Geophysical Research*, *115*, A02202. https://doi.org/10.1029/2009JA014522

Sergeev, V. A., & Tsyganenko, N. A. (1982). Energetic particle losses and trapping boundaries as deduced from calculations with a realistic magnetic field model. *Planetary and Space Science*, *30*, 999–1006. https://doi.org/10.1016/0032-0633(82)90149-0

Sergeev, V. A., & Yahnin, A. G. (1979). The features of auroral bulge expansion. *Planetary and Space Science*, *27*, 1429–1440. https://doi.org/10.1016/0032-0633(79)90089-8

Shabansky, V. P. (1971). Some processes in the magnetosphere. *Space Science Reviews*, *12*(3), 299–418. https://doi.org/10.1007/bf00165511

Shiokawa, K., Katoh, Y., Hamaguchi, Y., Yamamoto, Y., Adachi, T., Ozaki, M., et al. (2017). Ground-based instruments of the PWING project to investigate dynamics of the inner magnetosphere at subauroral latitudes as a part of the ERG-ground coordinated observation network. *Earth, Planets and Space*, *69*(1), 160. https://doi.org/10.1186/s40623-017-0745-9

Shreedevi, P. R., Yu, Y., Ni, B., Saikin, A., & Jordanova, V. K. (2021). Simulating the ion precipitation from the inner magnetosphere by H-band and He-band electro magnetic ion cyclotron Waves. *Journal of Geophysical Research: Space Physics*, *126*, e2020JA028553. https://doi.org/10.1029/2020JA028553

Smith, P. H., & Hoffman, R. A. (1974). Direct observations in the dusk hours of the characteristics of the storm time ring current particles during the beginning of magnetic storms. *Journal of Geophysical Research*, *79*(7), 966–971. https://doi.org/10.1029/ja079i007p00966

Søraas, F., Lundblad, J. A., Maltseva, N. F., Troitskaya, V. A., & Selivanov, V. (1980). A comparison between simultaneous IPDP ground-based observations of energetic protons obtained by satellites. *Planetary and Space Science*, *28*, 387–405. https://doi.org/10.1016/0032-0633(80)90043-4

Summers, D. (2005). Quasi-linear diffusion coefficients for field-aligned electromagnetic waves with applications to the magnetosphere. *Journal of Geophysical Research*, *110*, A08213. https://doi.org/10.1029/2005JA011159

Thorne, R. M., & Kennel, C. F. (1971). Relativistic electron precipitation during magnetic storm main phase. *Journal of Geophysical Research*, *76*(19), 4446–4453. https://doi.org/10.1029/JA076i019p04446

Trakhtengerts, V. Y., & Rycroft, M. J. (2008). *Whistler and Alfvén mode cyclotron masers in space. Cambridge Atmospheric and Space Sciences Series*. Cambridge University Press.

Tsyganenko, N. A. (1989). A magnetospheric magnetic field model with a warped tail current sheet. *Planetary and Space Science*, *37*(1), 5–20. https://doi.org/10.1016/0032-0633(89)90066-4

Usanova, M. E., & Mann, I. R. (2016). Understanding the role of EMIC waves in radiation belt and ring current dynamics: Recent advances. In G. Balasis, I. A. Daglis, & I. R. Mann (Eds.), *Waves, particles, and storms in geospace: A complex interplay*. Oxford University Press. https://doi.org/10.1093/acprof:oso/9780198705246.003.0011

Usanova, M. E., Mann, I. R., Bortnik, J., Shao, L., & Angelopoulos, V. (2012). THEMIS observations of electromagnetic ion cyclotron wave occurrence: Dependence on AE, SYMH, and solar wind dynamic pressure. *Journal of Geophysical Research*, *117*, A10218. https://doi.org/10.1029/2012JA018049

Usanova, M. E., Mann, I. R., Kale, Z. C., Rae, I. J., Sydora, R. D., Sandanger, M., et al. (2010). Conjugate ground and multisatellite observations of compression-related EMIC Pc1 waves and associated proton precipitation. *Journal of Geophysical Research*, *115*, A07208. https://doi.org/10.1029/2009JA014935

Vallat, C., Ganushkina, N., Dandouras, I., Escoubet, C. P., Taylor, M. G. G. T., Laakso, H., et al. (2007). Ion multi-nose structures observed by Cluster in the inner Magnetosphere. *Annales Geophysicae*, *25*, 171–190. https://doi.org/10.5194/angeo-25-171-2007

Williams, D. J., & Lyons, L. R. (1974). Further aspects of the proton ring current interaction with the plasmapause: Main and recovery phases. *Journal of Geophysical Research*, *79*(31), 4791–4798. https://doi.org/10.1029/ja079i031p04791

Wygant, J. R., Bonnell, J. W., Goetz, K., Ergun, R. E., Mozer, F. S., Bale, S. D., et al. (2013). The electric field and waves instruments on the radiation belt storm probes mission. *Space Science Reviews*, *179*, 123–220. https://doi.org/10.1007/s11214-013-0013-7

Xiong, Y., Yuan, Z., & Wang, J. (2016). Energetic ions scattered into the loss cone with observations of the Cluster satellite. *Annales Geophysicae*, *34*, 249–257. https://doi.org/10.5194/angeo-34-249-2016

Yahnin, A. G., Bosinger, T., Belian, R. D., Bräysy, T., Mursula, K., & Singer, H. J. (1996). Energy spectra of protons and electrons in two longitudinally separate parts of a substorm injection region. *Cosmic Research*, *34*(5), 432–437.

Yahnin, A. G., Sergeev, V. A., Pellinen, R. J., Baumjohann, W., Kaila, K. U., Ranta, H., et al. (1983). Substorm time sequence and microstructure on 11 November 1976. *Journal of Geophysics*, *53*, 182–197.

Yahnin, A. G., Titova, E. E., Demekhov, A. G., Yahnina, T. A., Popova, T. A., Lyubchich, A., et al. (2019). Simultaneous observations of EMIC waves, ELF/VLF waves, and energetic particle precipitation during multiple compressions of the magnetosphere. *Geomagnetism and Aeronomy*, *59*, 668–680. https://doi.org/10.1134/S0016793219060148

Yahnin, A. G., & Yahnina, T. A. (2007). Energetic proton precipitation related to ion–cyclotron waves. *Journal of Atmospheric and Solar-Terrestrial Physics*, *69*, 1690–1706. https://doi.org/10.1016/j.jastp.2007.02.010

Yahnin, A. G., Yahnina, T. A., Frey, H. U., Bösinger, T., & Manninen, J. (2009). Proton aurora related to intervals of pulsations of diminishing periods. *Journal of Geophysical Research*, *114*, A12215. https://doi.org/10.1029/2009JA014670

Yahnin, A. G., Yahnina, T. A., Semenova, N. V., Popova, T. A., & Demekhov, A. G. (2018). Proton auroras equatorward of the oval as a manifestation of the ion-cyclotron instability in the Earth's magnetosphere (brief review). *Geomagnetism and Aeronomy*, *58*(5), 577–585. https://doi.org/10.1134/S001679321805016X

Yahnina, T. A., Yahnin, A. G., Kangas, J., Manninen, J., Evans, D. S., Demekhov, A. G., et al. (2003). Energetic particle counterparts for geomagnetic pulsations of Pc1 and IPDP types. *Annales Geophysicae*, *21*, 2281–2292. https://doi.org/10.5194/angeo-21-2281-2003

Yando, K., Millan, R. M., Green, J. C., & Evans, D. S. (2011). A Monte Carlo simulation of the NOAA POES medium energy proton and electron detector instrument. *Journal of Geophysical Research*, *116*, A10231. https://doi.org/10.1029/2011JA016671

Yokota, S., Kasahara, S., Hori, T., Keika, K., Miyoshi, Y., & Shinohara, I. (2019). The MEP-i instrument Level-2 3-D flux data of Exploration of energization and Radiation in Geospace (ERG) Arase satellite. Version v01_02, updated daily. ERG Science Center, Institute for Space-Earth Environmental Research, Nagoya University. https://doi.org/10.34515/DATA.ERG-03000

Yokota, S., Kasahara, S., Mitani, T., Asamura, K., Hirahara, M., Takashima, T., et al. (2017). Medium-energy particle experiments–ion mass analyzer (MEP-i) onboard ERG (Arase). *Earth, Planets and Space*, *69*, 172. https://doi.org/10.1186/s40623-017-0754-8

Yue, C., Bortnik, J., Thorne, R. M., Ma, Q., An, X., Chappell, C. R., & Kletzing, C. A. (2017). The characteristic pitch angle distributions of 1 eV to 600 keV protons near the equator based on Van Allen Probes observations. *Journal of Geophysical Research: Space Physics*, *122*, 9464–9473. https://doi.org/10.1002/2017JA024421

Zhang, J.-C., Saikin, A. A., Kistler, L. M., Smith, C. W., Spence, H. E., Mouikis, C. G., et al. (2014). Excitation of EMIC waves detected by the Van Allen Probes on 28 April 2013. *Geophysical Research Letters*, *41*, 4101–4108. https://doi.org/10.1002/2014GL060621

Zhang, Y., & Paxton, L. J. (2008). An empirical *Kp*-dependent global auroral model based on TIMED/GUVI FUV data. *Journal of Atmospheric and Terrestrial Physics*, *70*(8–9), 1231–1242. https://doi.org/10.1016/j.jastp.2008.03.008

Zhang, Y., Shi, R., Ni, B., Gu, X., Zhang, X., Zuo, P., et al. (2017). Inferring electromagnetic ion cyclotron wave intensity from low altitude POES proton flux measurements: A detailed case study with conjugate Van Allen Probes observations. *Advances in Space Research*, *59*(6), 1568–1576. https://doi.org/10.1016/j.asr.2016.12.035